약학박사 학위논문

Structural studies on the non-translational function of human asparaginyl-tRNA synthetase as a novel chemokine targeting CCR3

CCR3 를 통한 염증 신호를 일으키는 NRS N 말단 부위에 대한 구조생물학적 연구

2019 년 2 월

서울대학교 대학원
약학과 의약생명과학전공
박 준 성

Abstract

Structural studies on the non-translational function of human asparaginyl-tRNA synthetase as a novel chemokine targeting CCR3

Joon Sung Park

Division of Pharmaceutical Bioscience

College of Pharmacy

The Graduate School

Seoul National University

Asparaginyl-tRNA synthetase (NRS) is not only essential in protein translation but also associated with autoimmune diseases. Particularly, patients with antibodies that recognize NRS often develop interstitial lung disease (ILD). However, the underlying mechanism of how NRS is recognized by immune cells and provokes inflammatory responses is not well-understood. Here, I found that

the crystal structure of the unique N-terminal extension domain of human NRS (named as UNE-N, where -N denotes NRS) resembles that of the chemotactic N-terminal domain of NRS from a filarial nematode, *Brugia malayi*, which recruits and activates specific immune cells by interacting with CXC chemokine receptor 1 and 2. UNE-N induced migration of C-C chemokine receptor 3 (CCR3)-expressing cells. The chemokine activity of UNE-N was significantly reduced by suppressing CCR3 expression with CCR3-targeting siRNA, and the loop3 region of UNE-N was shown to interact mainly with the extracellular domains of CCR3 in nuclear magnetic resonance perturbation experiments. Based on these results, evolutionarily acquired UNE-N elicits chemokine activities that would promote NRS-CCR3-mediated proinflammatory signaling in ILD.

Keywords: Human asparaginyl-tRNA synthetase (NRS), chemokine, CC chemokine receptor 3 (CCR3), X-ray crystallography, antisynthetase syndrome

Student Number: 2012-21588

Table of Contents

Abstract i

Table of Contents iii

List of Tables v

List of Figures vi

Abbreviations viii

1. Introduction 1

1.1. Aminoacyl-tRNA synthetase 1
1.2. Class 2b ARS 10
1.3. Chemokine activities of NRS 12
1.4. Antisynthetase syndrome 14
1.5. Chemokine 16
1.6. Summary 18

2. Materials and Methods 19

2.1. Cloning, protein expression, and purification 19
2.2. Selenomethionine incorporation 28
2.3. Crystallography 28
2.4. NMR analysis 35
2.5. Cell culture 36
2.6. Cell migration assay 37

2.7. Secretion assay 38
2.8. Immunoblotting 39
2.9. Pull-down assay 39
2.10. Statistical analysis 40
2.11. Data deposition 40

3. Results 41

3.1. UNE-N shares a structural scaffold with the chemotactic N-terminal domain of *Bm*NRS but exhibits unique features 41
3.2. Th1 and Th2 cytokines induce NRS secretion from macrophages 56
3.3. UNE-N exclusively elicits chemotactic activities of NRS on Daudi and Jurkat cells 60
3.4. UNE-N directly interacts with CCR3 extracellular domains 64
3.5. Loop3 of UNE-N is an effector motif for CCR3 interactions 68
3.6. Loop3 region of UNE-N is structurally distinct from UNE-N of *Bm*NRS targeting different receptors 75

4. Discussion 79

5. References 88

6. Abstract in Korean (국문 초록) 96

List of Tables

Table 1 Classification of ARSs..... 3

Table 2 Statistics on data collection and refinement..... 34

Table 3 NMR chemical shift−based prediction for the secondary structure of UNE−N using the TALOS+ program..... 46

List of Figures

Figure 1 Two steps of tRNA aminoacylation catalyzed by ARSs.. 2

Figure 2 Conserved structures of class 1 and class 2 ARSs..... 5

Figure 3 Non-translational functions of recombinant ARSs 7

Figure 4 Splice variants of mammalian ARSs 8

Figure 5 Schematic representation of the organization of MSC 9

Figure 6 Crystal structure of DRS..... 11

Figure 7 Solution structure of UNE-N of *Bm*NRS..... 13

Figure 8 Distributions of clinical diagnoses in patients with anti-ARS antibodies 15

Figure 9 Typical structure of a chemokine..... 17

Figure 10 Secondary-structure prediction on NRS with the XtalPred server 21

Figure 11 Purification of full-length NRS..... 22

Figure 12 Purification of CD 23

Figure 13 Purification of UNE-N..... 25

Figure 14 Purification of MBP fused CCR3 ED3..... 27

Figure 15 Crystals of UNE-N and their x-ray diffraction..... 30

Figure 16 Crystals of CD and their x-ray diffraction..... 32

Figure 17 Domain composition of NRS..... 43

Figure 18 Crystal structure of UNE-N 44

Figure 19 Hetero-nuclear $^{1}H-^{15}N$ NOE data of UNE-N 49

Figure 20 Dynamics of UNE-N obtained from CLEANEX-PM spectra 50

Figure 21 CLEANEX-PM spectrum represented on crystal structure of UNE-N 51

Figure 22 Comparison of $^{1}H-^{15}N$ HSQC spectra of UNE-N and $UNE-N_{111}$ 53

Figure 23 Crystal structure of CD 55

Figure 24 Secretion of NRS from macrophages 57

Figure 25 Induction of NRS secretion by cytokines 59

Figure 26 Chemokine activity of UNE-N 61

Figure 27 NRS induces chemotaxis, not chemokinesis 63

Figure 28 CCR3 mediates chemokine activity of NRS 65

Figure 29 Direct interaction of UNE-N with CCR3 67

Figure 30 Key residues of UNE-N involved in the interaction with CCR3 70

Figure 31 Chemical shift perturbations of UNE-N upon binding to CCR3 ED3 72

Figure 32 Chemical shift perturbations of UNE-N upon binding to CCR3 ED1 74

Figure 33 Sequence alignment of UNE-Ns from nine eukaryotic NRSs 76

Figure 34 Residues on $\beta 2$-loop3-$\beta 3$ regions of UNE-Ns of human and *B. malayi* 78

Figure 35 Residues on loop2 and $\alpha 2$ regions of UNE-Ns of human and *B. malayi* 84

Figure 36 Backbone RMSD and $^{15}N-^{1}H$ hetero-nuclear NOE values of UNE-N of *Bm*NRS plotted against residue number . 85

Abbreviations

ABD	Anticodon-binding domain
AIMP1/2/3	Aminoacyl-tRNA synthase complex-interacting multifunctional protein 1/2/3
ARS	Aminoacyl-tRNA synthetase
CCL5	C-C chemokine ligand 5, RANTES
CCL11	C-C chemokine ligand 11, eotaxin-1
CCR3/5	C-C chemokine receptor 3/5
CD	Canonical domain of NRS
CD4/8	Cluster of differentiation 4/8
CLEANEX-PM	Phase-modulated CLEAN chemical exchange
CXCR1/2	CXC chemokine receptor 1/2
ED1/2/3/4	Extracellular domain 1/2/3/4
HR	Hinge region
HSQC	Heteronuclear single quantum coherence
iDC	Immature dendritic cells
ILD	Interstitial lung disease
INF-γ	Interferon-γ
MBP	Maltose binding protein
MSC	Multi-aminoacyl-tRNA synthetase complex
NMR	Nuclear magnetic resonance
NOE	Nuclear Overhauser effect
NRS	Asparaginyl-tRNA synthetase
PBS	Phosphate buffered saline
RMSD	Root-mean-square deviation

SAD	Single anomalous diffraction
S/N	Signal to noise
TCA	Trichloroacetic acid
TEV protease	Tobacco etch virus protease
TGF-β	Transforming growth factor-β
Th1	T-helper 1
Th2	T-helper 2
TNF-α	Tumor necrosis factor-α
UNE-N	Unique N-terminal extension domain of NRS

1. Introduction

1.1 Aminoacyl-tRNA synthetase

Aminoacyl-tRNA synthetases (ARSs) play a fundamental role in protein synthesis by charging tRNAs with matching amino acids. Their reaction is composed of two steps; the first step is formation of aminoacyl-AMP by consuming ATP to AMP and the second step is conjugation of the aminoacyl moiety to tRNA (Fig. 1). ARSs could be classified into two classes; class 1 and class 2 based on their catalytic mechanisms and structures[1-4] (Table 1).

Step 1.

amino acid + ATP → aminoacyl-AMP + PPi

Step 2.

aminoacyl-AMP + tRNA → aminoacyl-tRNA + AMP

Figure 1. Two steps of tRNA aminoacylation catalyzed by ARSs.

Table 1. Classification of ARSs[3].

Class	Subclass	ARS (Form)	Organism	PDB ID
1	a	Isoleucyl−tRNA synthetase (α)	*Thermus thermophilus*	1ILE
		Methionyl−tRNA synthetase (α2)	*Thermus thermophilus*	1A8H
		Leucyl−tRNA synthetase (α)	*Thermus thermophilus*	1H3N
		Valyl−tRNA synthetase (α)	*Thermus thermophilus*	1GAX
	b	Cysteinyl−tRNA synthetase (α)	*Escherichia coli*	1LI5
		Glutaminyl−tRNA synthetase (α)	*Saccharomyces cerevisiae*	4H3S
		Glutamyl−tRNA synthetase (α)	*Thermus thermophilus*	1J09
	c	Tyrosyl−tRNA synthetase (α2)	*Thermus thermophilus*	1H3F
		Tryptophanyl−tRNA synthetase (α2)	*Homo sapiens*	2AKE
	d	Arginyl−tRNA synthetase (α)	*Thermus thermophilus*	1IQ0
	e	Lysyl−tRNA synthetase Ⅰ (α)	*Pyrococcus horikoshii*	1IRX
2	a	Glycyl−tRNA synthetase (α2)	*Thermus thermophilus*	1ATI
		Histidyl−tRNA synthetase (α2)	*Escherichia coli*	1HTT
		Prolyl−tRNA synthetase (α2)	*Plasmodium falciparum*	4TWA
		Seryl−tRNA synthetase (α2)	*Methanosarcina barkeri*	2CJB
		Threonyl−tRNA synthetase (α2)	*Escherichia coli*	1QF6
	b	Asparaginyl−tRNA synthetase (α2)	*Brugia malayi*	2XGT
		Aspartyl−tRNA synthetase(α2)	*Saccharomyces cerevisiae*	1ASY
		Lysyl−tRNA synthetase Ⅱ (α2)	*Homo sapiens*	4YCU
	c	Alanyl−tRNA synthetase (α4)	*Archaeoglobus fulgidus*	3WQY
		Glycyl−tRNA synthetase (α2β2)	*Homo sapiens*	2ZT5
		Phenylalanyl−tRNA synthetase (α2β2)	*Thermus thermophilus*	1B70
		Pyrolysyl−tRNA synthetase (α2)	*Methanosarcina mazei*	2Q7H

Each class 1 ARS features a Rossman fold that comprises a parallel β-sheet in its nucleotide binding site. In addition, class 1 ARSs share the mechanism of reaction that initially attaches an amino acid to 2′ -OH of the target adenosine and sequentially transfers the amino acid to 3′ -OH of the adenosine. Class 2 ARSs commonly have anti-parallel β-sheets in their nucleotide binding sites and directly attach amino acids to 3′ -OH of their substrate adenosines[2] (Fig. 2).

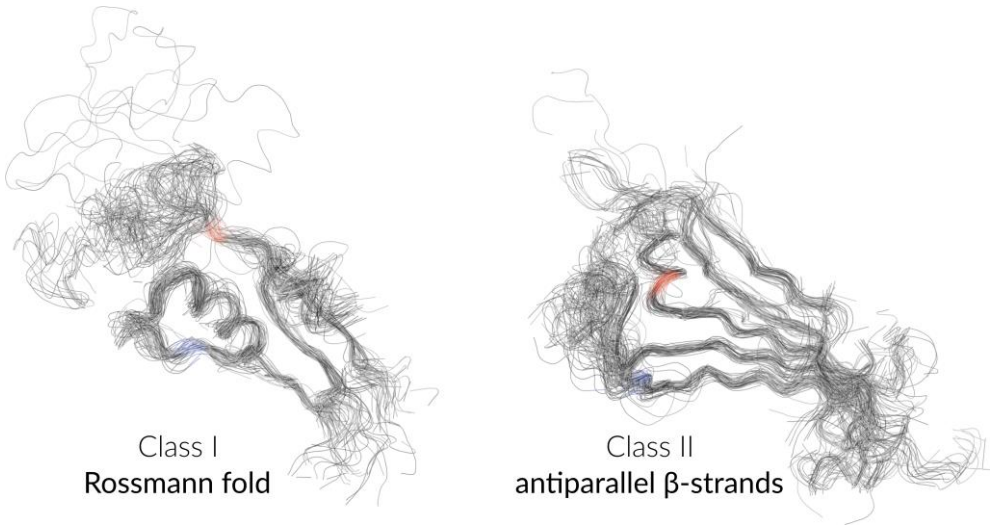

Figure 2. Conserved structures of class 1 and class 2 ARSs. Structural alignment of catalytic domains of class 1 and class 2 ARSs shows shared Rossman folds and anti-parallel β-sheet structures, respectively. N- and C-termini of backbone brackets in class 1 ARSs and arginine tweezers in class 2 ARSs are colored in blue and red, respectively. (Source: adapted from "Alignment of the core domains of aminoacyl-tRNA synthetases class I and class II" by Enauz. (CC BY-SA 4.0), https://en.wikipedia.org/wiki/Aminoacyl_tRNA_synthetase#/media/File:Aars_alignment.png)

In addition to translational functions, higher eukaryotic ARSs are known to play roles in various physiological events such as vascular development, angiogenesis, cytokine signaling, tumorigenesis, inflammation, apoptosis, neural development, and immunological response via their evolutionarily acquired domains and alternative splicing variants of catalytic nulls[5-8] (Fig. 3 and Fig. 4). Higher eukaryotes have also developed a multi-aminoacyl-tRNA synthetase complex (MSC) that serves as a reservoir and regulatory machinery of translational or non-translational functions of the component ARSs[5,9,10] (Fig. 5).

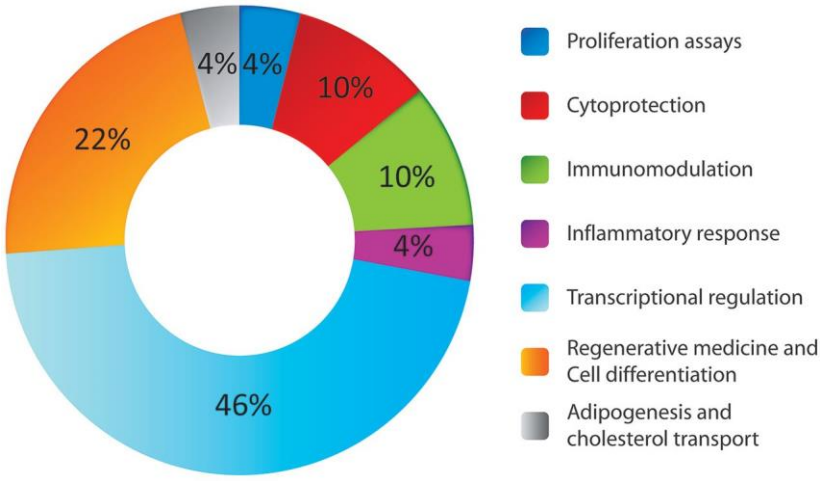

Figure 3. Non-translational functions of recombinant ARSs. Recombinant ARS variants were tested in cell-based assays, which showed that the ARS variants are involved in a variety of biological events. (From Lo, W. S. et al. Human tRNA synthetase catalytic nulls with diverse functions. *Science* 345, 328-332, doi:10.1126/science.1252943 (2014). Reprinted with permission from AAAS)

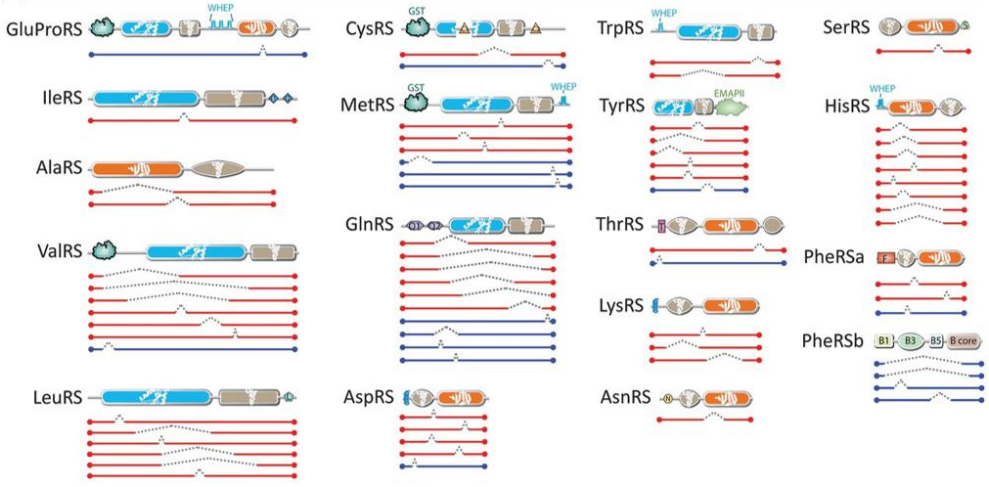

Figure 4. Splice variants of mammalian ARSs. Catalytic domains are abrogated in most splice variants of ARSs but domains involved in non-translational function are predominantly retained. (From Lo, W. S. et al. Human tRNA synthetase catalytic nulls with diverse functions. *Science* 345, 328-332, doi:10.1126/science.1252943 (2014). Reprinted with permission from AAAS)

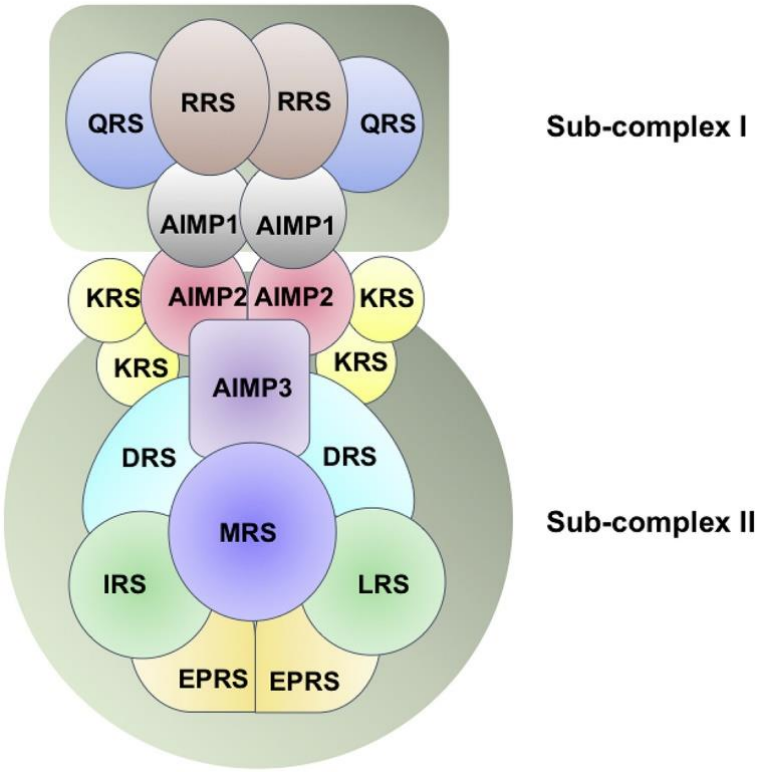

Figure 5. Schematic representation of the organization of MSC. A human MSC is composed of nine different ARSs and three auxiliary proteins (AIMP1, 2, and 3) in mammals. EPRS, glutamyl-prolyl-tRNA synthetase; IRS, isoleucyl-tRNA synthetase; LRS, leucyl-tRNA synthetase; MRS, methionyl-tRNA synthetase; QRS, glutaminyl-tRNA synthetase; KRS, lysyl-tRNA synthetase; RRS, arginyl-tRNA synthetase; DRS, aspartyl-tRNA synthetase; AIMP, aminoacyl-tRNA synthase complex-interacting multifunctional protein. (Reprinted from Rajendran, V. et al. Aminoacyl-tRNA synthetases: Structure, function, and drug discovery. *Int J Biol Macromol* 111, 400-414, doi:10.1016/j.ijbiomac.2017.12.157 (2018), with permission from Elsevier)

1.2. Class 2b ARS

NRS, DRS, and KRS are classified as class 2b ARSs that share sequence motifs in their canonical domains (CD) which are composed of an anticodon-binding domain (ABD), a hinge region (HR), and a catalytic domain[11] (Fig. 6). Class 2b ARSs feature homodimeric assembly and eukaryote-specific N-terminal extension domains which modulate the bindings of substrate tRNAs with their lysine-rich x**SK**xx**LKK**xx**K** helical motifs[11-17]. In humans, the unique N-terminal extension domain of NRS (named as UNE-N where -N denotes NRS) is about 100 amino acids, which is longer than those of DRS (about 20 amino acids) and KRS (about 70 amino acids).

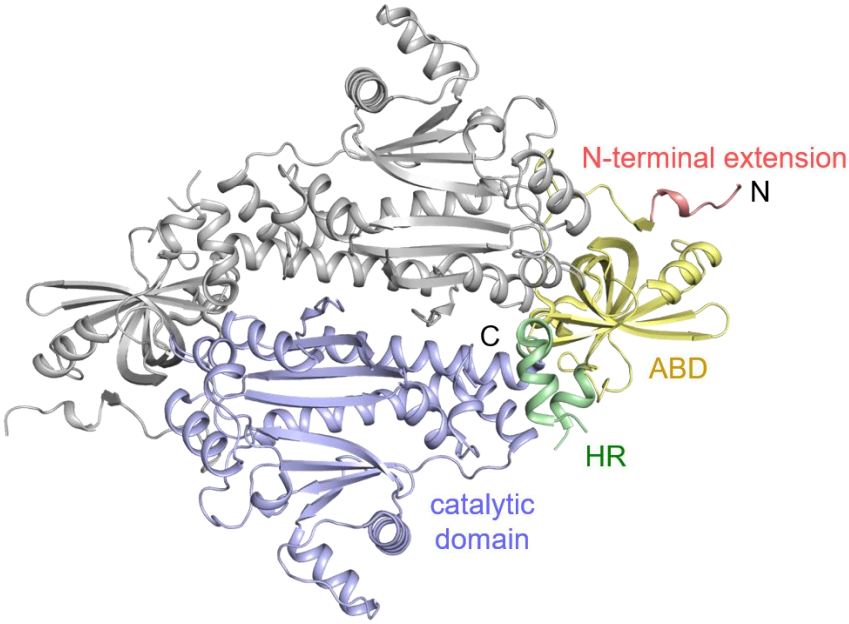

Figure 6. Crystal structure of DRS. Crystal structure of DRS is shown in cartoon representation (PDB ID: 4J15). DRS is one of class 2b ARSs and forms a homodimer. It has a modular structure with an N-terminal extension domain, an ABD, an HR, and a catalytic domain. The homodimeric partner molecule is colored in gray[17].

1.3. Chemokine activities of NRS

NRSs from human and *Brugia malayi* were reported to have chemokine activities[18,19]. Human NRS could induce migration of immune cells such as immature dendritic cells and lymphocytes through CCR3-mediated signaling. *B. malayi* is an infectious nematode causing filariasis in humans and it secrets a large amount of *Brugia malayi* NRS (*Bm*NRS) during infection. The secreted *Bm*NRS participates in the development of pathological responses by its interleukin 8 (IL-8)-like activities which modulate the host immune system[19-22] and stimulates endothelial cell proliferation, vasodilation, and angiogenesis[23]. *Bm*NRS also induces the migration of immune cells that is mediated by CXC chemokine receptor 1 (CXCR1) and 2 (CXCR2)[19,22]. Based on the structural similarity to IL-8 and stromal cell derived factor-1, the hairpin-helix structure in UNE-N of *Bm*NRS was suggested as the effector motif for its receptor recognition[16,22] (Fig. 7).

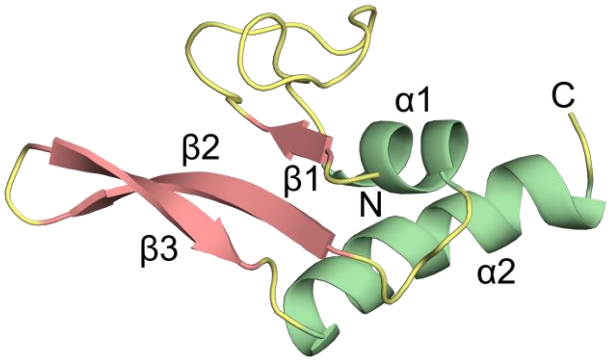

Figure 7. Solution structure of UNE-N of *Bm*NRS. Structure of UNE-N of *Bm*NRS (Met1-Glu74, PDB ID: 2KQR) is shown in cartoon representation. α-helices, β-strands, and loops are colored in palegreen, salmon, and yellow, respectively. UNE-N of *Bm*NRS contains a hairpin-helix motif, $\beta 2-\beta 3-\alpha 2$, which was suggested as the crucial motif to the chemokine activities.

1.4. Antisynthetase syndrome

Autoantibodies against eight ARSs have been identified in antisynthetase syndrome associated with interstitial lung disease (ILD) and idiopathic inflammatory myopathies: anti-Jo-1 (HRS), anti-PL-7 (threonyl-tRNA synthetase), anti-PL-12 (alanyl-tRNA synthetase), anti-OJ (IRS), anti-EJ (glycyl-tRNA synthetase), anti-KS (NRS), anti-Ha (tyrosyl-tRNA synthetase), and anti-Zo (phenylalanyl-tRNA synthetase)[24-26] (Fig. 8). Autoantibody-targeted ARSs are released in specific immune conditions and some of them have been known to elicit chemotactic activities[18,27,28]. Anti-Jo-1, autoantibodies to HRS, is most frequently observed in antisynthetase syndrome, and HRS has been shown to induce migration of $CD4^+$ (cluster of differentiation 4) and $CD8^+$ (cluster of differentiation 8) lymphocytes, interleukin-2-activated monocytes, and immature dendritic cells (iDCs) in a CC chemokine receptor (CCR) 5-dependent manner. Similarly, anti-KS, autoantibodies to NRS, is often detected in patients with ILD[26] and NRS recruits iDCs and immune cells in a CCR3-dependent manner[18].

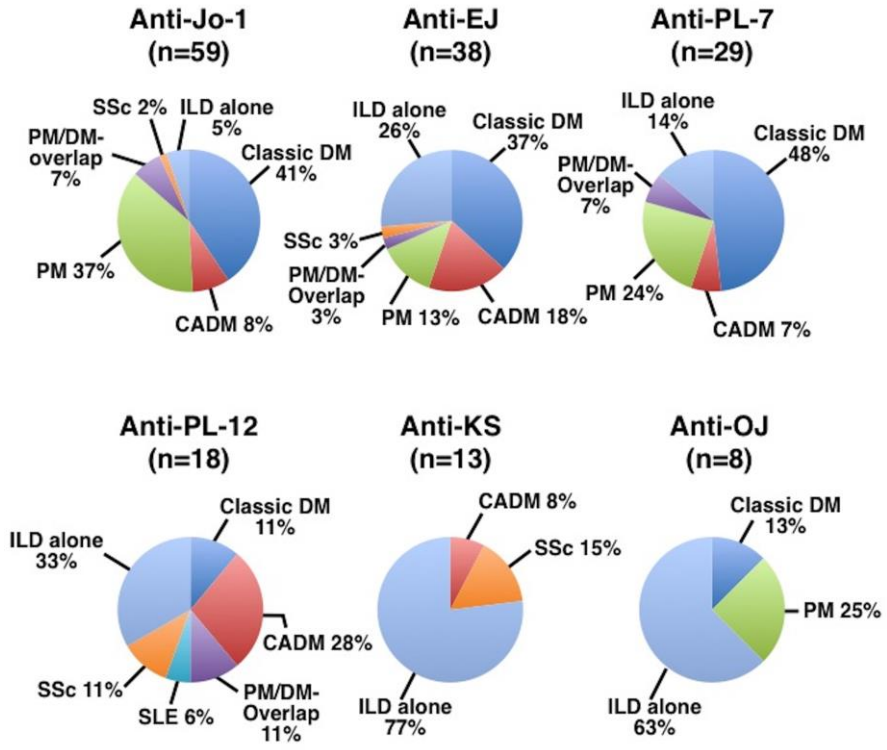

Figure 8. Distributions of clinical diagnoses in patients with anti-ARS antibodies. The patients with anti-KS showed the most dominant prevalence (77%) of ILD alone. DM, dermatomysitis; CADM, clinically amyopathic DM; PM, polymyositis; SLE, systemic lupus erythematosus; SSc, systemic sclerosis. (Source: adapted from Hamaguchi, Y. et al. Common and distinct clinical features in adult patients with anti-aminoacyl-tRNA synthetase antibodies: heterogeneity within the syndrome. *PLoS One* 8, e60442, doi:10.1371/journal.pone.0060442 (2013) (CC BY 4.0), https://doi.org/10.1371/journal.pone.0060442.g003)

1.5. Chemokine

Chemokines are the cytokines with chemotactic activities and classified into C, CC, CXC, and CX_3C chemokines based on the conserved motifs of cysteines that are participating in intramolecular disulfide bonds with other cysteines[29]. Typical structure of a chemokine contains an antiparallel β-sheet of three β-strands and a following C-terminal α-helix ($\beta1-\beta2-\beta3-\alpha1$), which forms the Greek key shape (Fig. 9). Chemokine receptors are also classified into XCR, CCR, CXCR, and CX_3CR receptors depending on the types of chemokines they recognize. They are the members of G-protein coupled receptor family that have seven transmembrane helices and four extracellular domains. CCL5 and CCL11 are the representative CC chemokines targeting CCR3 which mediates chemotactic activities in the CCR3-expressing cells like iDCs and lymphocytes[30].

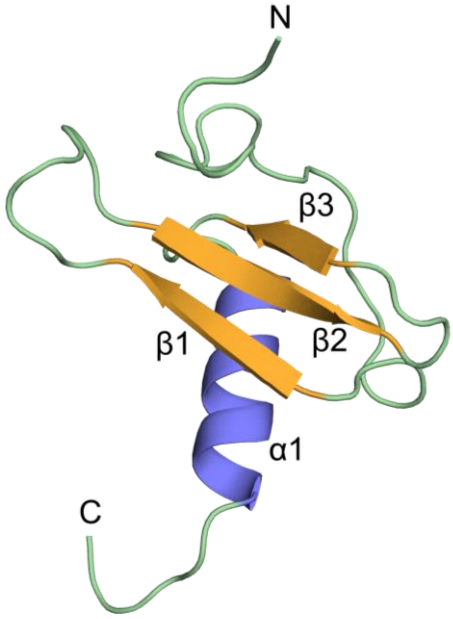

Figure 9. Typical structure of a chemokine. Solution structure of CCL11 is shown in cartoon representation (PDB ID: 1EOT).

1.6. Summary

So far, at least three reasonable manifestations of NRS-autoimmune disease relationship have been accumulated; 1) autoantibodies to NRS have been observed in the patients with ILD, 2) NRS can elicit CCR3-mediated signaling in specific immune conditions, and 3) UNE-N of *Bm*NRS, which is homologous to UNE-N of human, is able to recruit particular chemokine receptors to provoke pathological effects. To decipher the connections between NRS, CCR3, and autoimmune diseases at a molecular level, I determined the crystal structures of UNE-N and CD of NRS and further examined molecular dynamics of UNE-N that was speculated as an effector domain to CCR3. Several conditions for NRS secretion and chemokine activities of full-length NRS, UNE-N, and CD were tested. For further information of the direct interaction between NRS and CCR3, pull-down assays were implemented and NMR chemical shift changes of UNE-N in the absence and presence of each extracellular domain (ED) of CCR3 were measured through NMR perturbation experiments. In conclusion, I suggest that the evolutionarily acquired UNE-N could be a fundamental determinant of immunological importance, thus a niche for unraveling a complicated NRS-related autoimmune problem.

2. Materials and Methods

2.1. Cloning, protein expression, and purification

NRS constructs for CD (residues 98–548) and UNE–N variants (residues 1–77, 4–77, and 1–111) were designed based on secondary structure prediction with the XtalPred server[31] and structure of *Bm*NRS[16] (Fig. 10).

Full–length NRS and CD (residues 98–548) were cloned into the pET–28a(+) plasmid (Novagen, Madison, WI, USA) between the Nde1 and Xho1 restriction sites. Each construct contained an N–terminal hexahistidine tag. NRS and CD were overexpressed in the C41(DE3) and Solu–BL21, *Escherichia coli* (*E. coli*) strains, respectively. The transformed cells were grown at 37 ℃ to an OD_{600} of 0.5 in Luria–Bertani media containing kanamycin and protein expression was induced by 0.5 mM isopropyl β–D–1–thiogalactopyranoside. The cells were incubated for additional 8 h and then harvested by centrifugation at 6,000 $\times g$ for 10 min. The harvested cells were resuspended in buffer A (500 mM NaCl, 20 mM Tris–HCl, 35 mM imidazole, pH 7.5) with 1 mM phenylmethylsulfonyl fluoride and lysed by sonication. Lysed cells were centrifuged at 35,000 $\times g$ for 1 h. The resulting supernatants were filtered with a 0.45–μm syringe filter device (Sartorius,

Gottingen, Germany) and loaded onto a 5-mL HiTrap chelating HP column (GE Healthcare) which had been pre-charged with Ni^{2+} and equilibrated with buffer A. After washing with buffer A, the retained proteins were eluted by addition of an increasing gradient of buffer B (500 mM NaCl, 20 mM Tris-HCl, 1 M imidazole, pH 7.5). The proteins were loaded onto a HiPrep desalting 26/10 column (GE Healthcare) and eluted with buffer C (50 mM NaCl, 20 mM Tris-HCl, pH 7.5). The eluates were loaded onto a HiTrap 5-ml Q HP (GE Healthcare) column. The loaded column was washed with buffer C and the retained proteins were eluted with an increasing gradient of buffer D (1 M NaCl, 20 mM Tris-HCl, pH 7.5). The proteins were finally purified over a HiLoad 16/600 Superdex 200 pg (GE Healthcare) column with appropriate buffers: buffer E (200 mM NaCl, 10 mM Tris-HCl, pH 7.5) for crystallization and phosphate-buffered saline (PBS, 137 mM NaCl, 2.7 mM KCl, 4.3 mM Na_2HPO_4, 1.4 mM KH_2PO_4, pH 7.4) for cell migration assays.

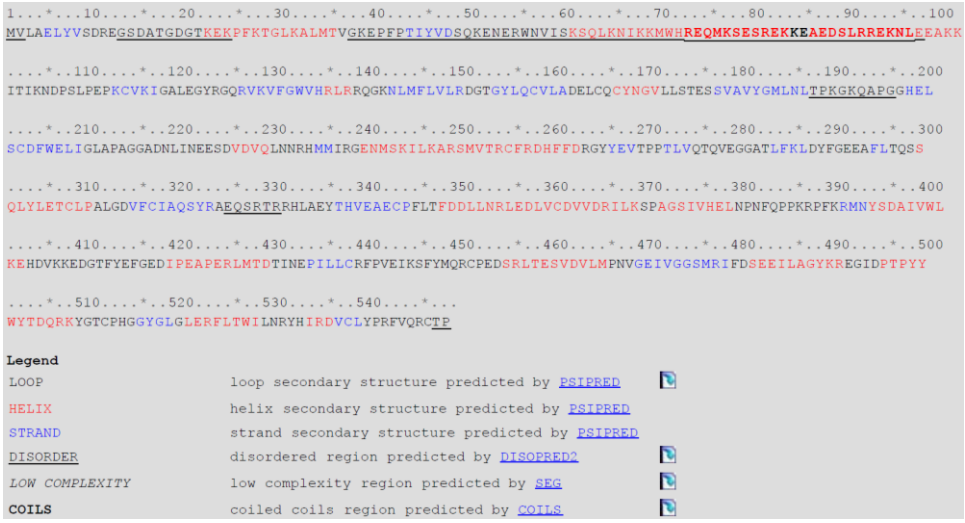

Figure 10. Secondary-structure prediction on NRS with the XtalPred server.

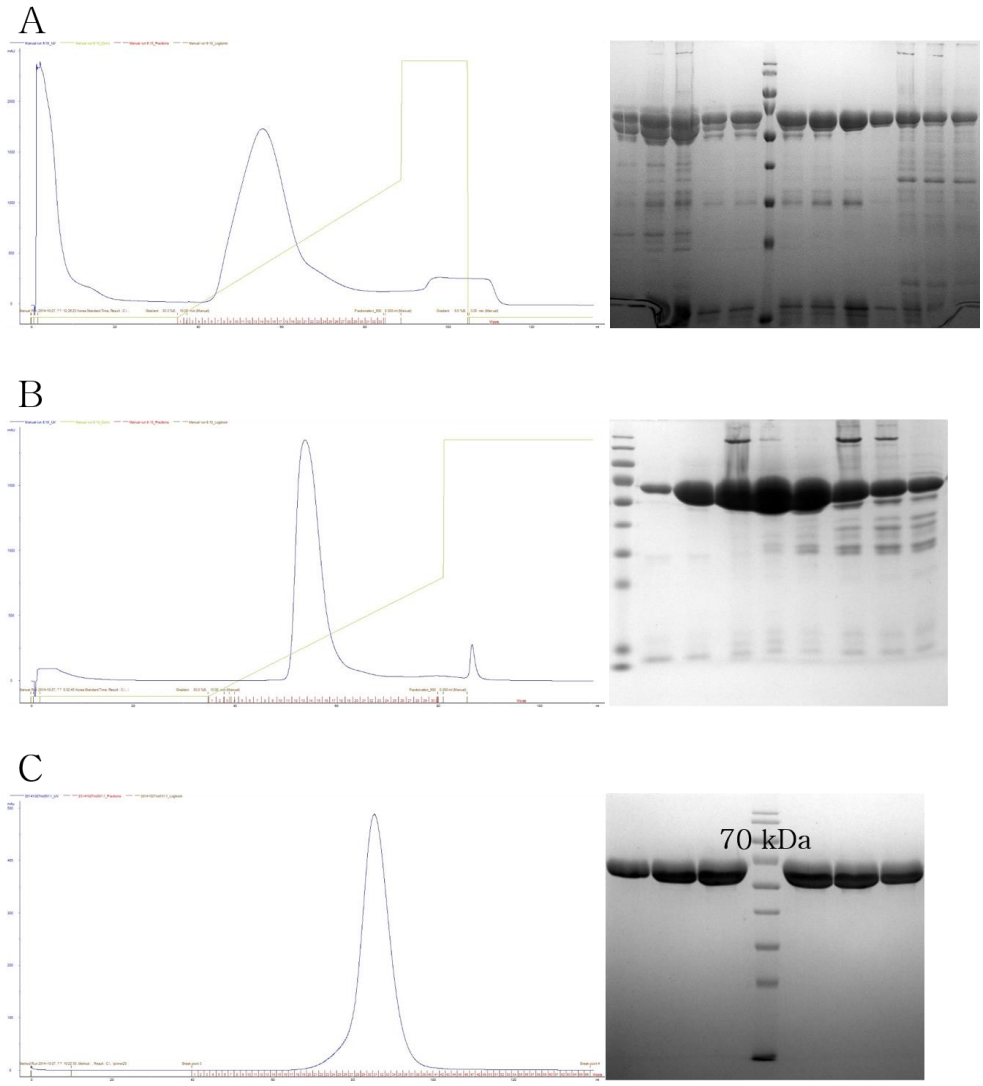

Figure 11. Purification of full-length NRS: Ni^{2+} affinity chromatography (A), anion exchange chromatography (B), and size exclusion chromatography (C). Purity of the protein fractions was checked by SDS-PAGE analysis after each purification step.

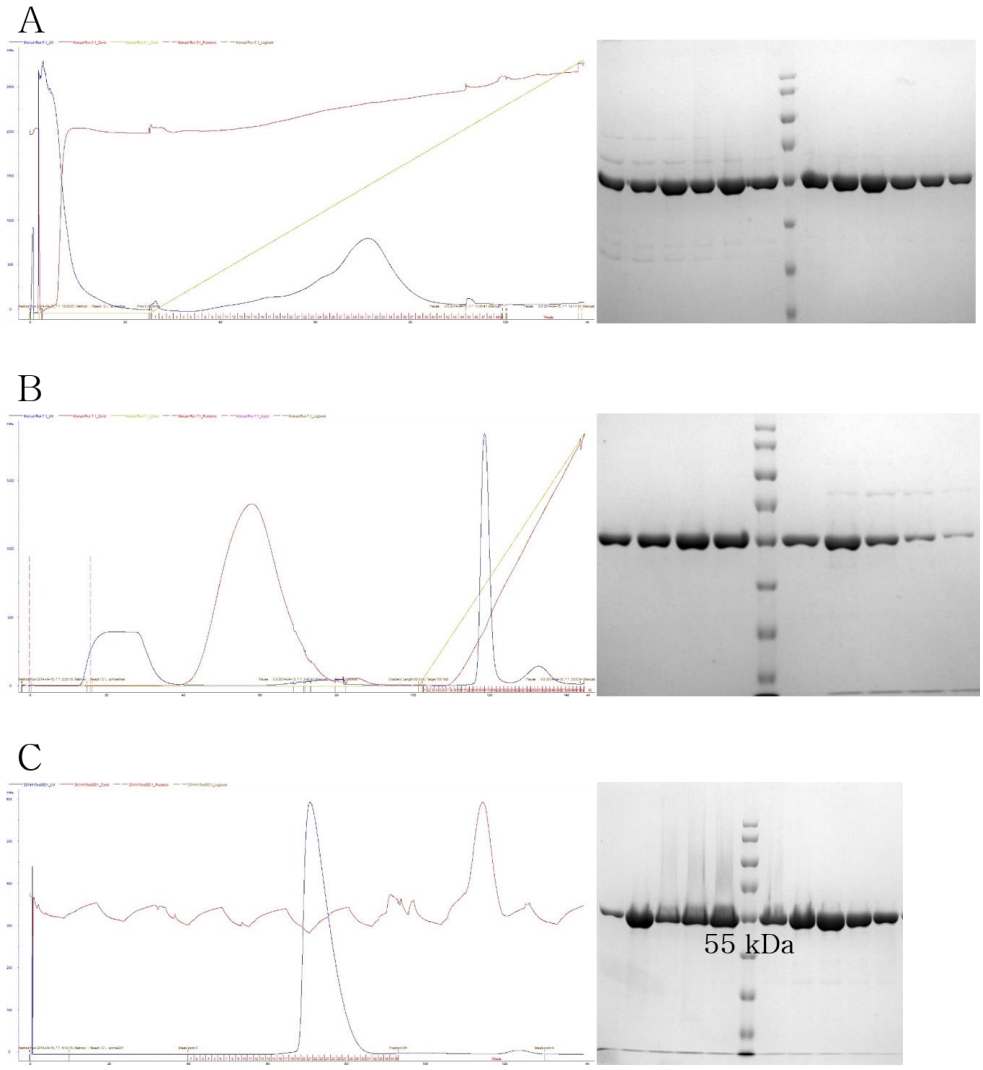

Figure 12. Purification of CD: Ni^{2+} affinity chromatography (A), anion exchange chromatography (B), and size exclusion chromatography (C). Purity of the protein fractions was checked by SDS-PAGE analysis after each purification step.

The UNE-N constructs were cloned into the pET-28a(+) plasmid between the Nde1 and Xho1 restriction sites. Each construct contained a hexahistidine tag, maltose binding protein (MBP), and tobacco etch virus (TEV) protease cleavage site at the N-terminus. Recombinant proteins were overexpressed in Rosetta 2(DE3), an *E. coli* strain. *E. coli* growth, protein expression, and purification up to hexahistidine tag affinity chromatography were same as the procedure used for NRS purification. The proteins purified by affinity chromatography were loaded onto a HiPrep desalting 26/10 column (GE Healthcare) and eluted with buffer E. The eluates were incubated with TEV protease at 4 ℃ overnight to cleave the MBP tag. The proteins were loaded onto a HiTrap 5-mL chelating HP column (GE Healthcare) pre-charged with Ni^{2+} and equilibrated with buffer E. The proteins in the flow-through fractions were loaded onto a HiLoad 16/600 Superdex 75 pg column (GE Healthcare) and eluted with appropriate buffers: buffer F (200 mM NaCl, 10 mM Tris-HCl, pH 8.5) for crystallization; PBS for cell migration assays; buffer G (150 mM NaCl, 20 mM NaH_2PO_4/Na_2HPO_4, pH 6.5), and buffer H (150 mM NaCl, 20 mM NaH_2PO_4/Na_2HPO_4, pH 7.5) for NMR experiments.

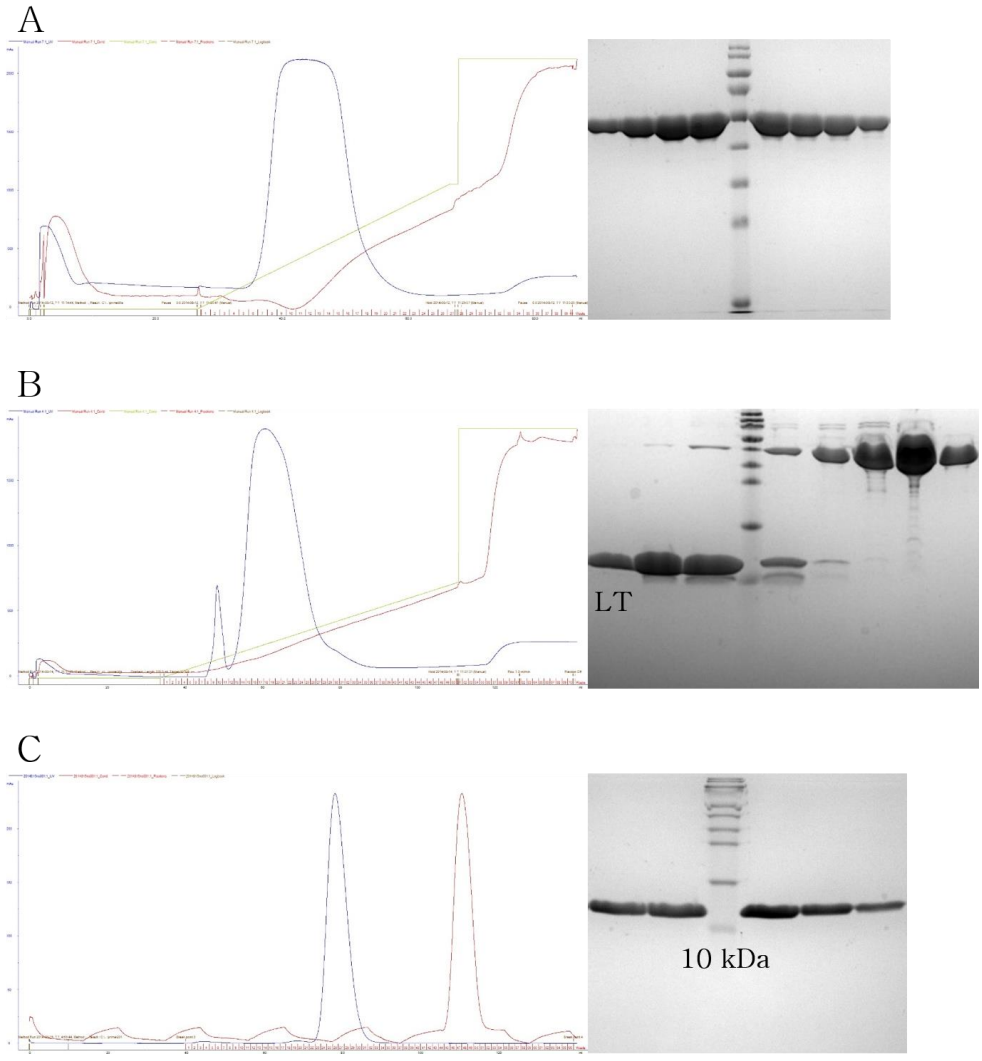

Figure 13. Purification of UNE-N: the first Ni^{2+} affinity chromatography (A), the second Ni^{2+} affinity chromatography after TEV protease treatment (B), and size exclusion chromatography (C). Purity of the protein fractions was checked by SDS-PAGE analysis after each purification step.

The four CCR3 ED sequences are as follows: ED1 (residues 1–40, MTTSLDTVET FGTTSYYDDV GLLCEKADTR ALMAQFVPPL), ED2 (residues 94–120, VRGHNWVFGH GMCKLLSGFY HTGLYSE), ED3 (residues 172–203, YETEELFEET LCSALYPEDT VYSWRHFHTL RM), and ED4 (residues 262–281, SSYQSILFGN DCERSKHLDL). MBP-fused CCR3 EDs were cloned into the pET-28a(+) plasmid between the Nde1 and Xho1 restriction sites. Each construct contained a hexahistidine tag at the N-terminus. Recombinant proteins were overexpressed in Rosetta 2(DE3), an *E. coli* strain. *E. coli* growth, protein expression, and purification steps up to hexahistidine tag affinity chromatography were same as those used for NRS purification. The proteins purified by affinity chromatography were loaded onto a HiLoad 16/600 Superdex 200 pg column (GE Healthcare) and eluted with appropriate buffers: PBS for pull-down assays and buffer H for NMR experiments.

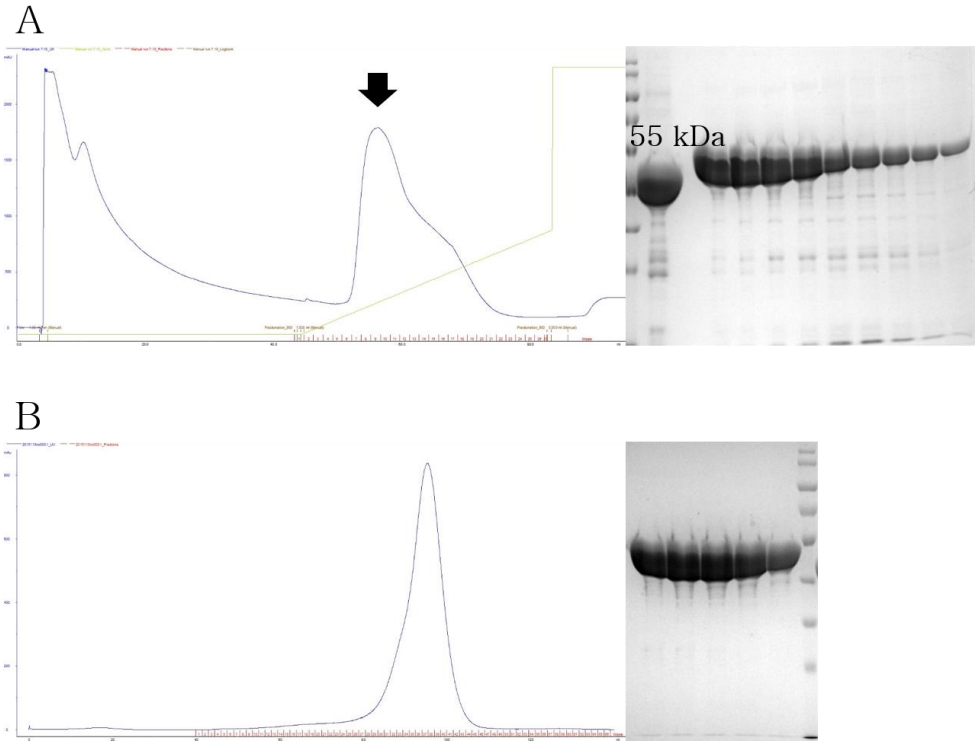

Figure 14. Purification of MBP fused CCR3 ED3: Ni^{2+} affinity chromatography (A) and size exclusion chromatography (B). Purity of the protein fractions was checked by SDS-PAGE analysis after each purification step.

2.2. Selenomethionine incorporation

For the selenomethionine-derived protein, UNE-N was overexpressed in B834(DE3), an *E. coli* strain. The cells were cultured in media containing M9, minimal salts (Sigma-Aldrich), and amino acid mix containing L-selenomethionine. Protein expression and purification were conducted in the same manner as native UNE-N purification.

2.3. Crystallography

Purified UNE-N and CD proteins were crystallized at 22 ℃ using the sitting drop vapor diffusion method with 1 μL protein and 1 μL crystallization solution. Initial crystals of UNE-N (residues 4-77) were grown under a commercial crystallization screening condition with 0.01 M zinc sulfate, 0.1 M MES (pH 6.5), and 25% (v/v) polyethylene glycol (PEG) 550 monomethyl ether (Structure Screen 2, Molecular Dimensions). Initial crystals were further optimized for x-ray diffraction data collection. The crystal was cryoprotected with the reservoir solution supplemented with 12.5% of glycerol and flash-cooled in a nitrogen gas stream at 100 K. Single-wavelength anomalous diffraction data were collected at the 5C beamline of Pohang Light Source, Republic of Korea, at an

anomalous peak wavelength (0.9796 Å). Collected data were processed at 1.9 Å resolution using the HKL2000 program suite[32]. The phase was solved by the single anomalous diffraction (SAD) method and an initial model was built using the AutoSol program of the PHENIX software package[33] and improved by density modification using the automatic model building program Resolve[34]. For the final model, another diffraction data set was collected from a selenomethionine-derived protein crystal and processed at 1.65 Å resolution. The model from the SAD method was used as a phasing template for molecular replacement implemented with the Phaser program[35].

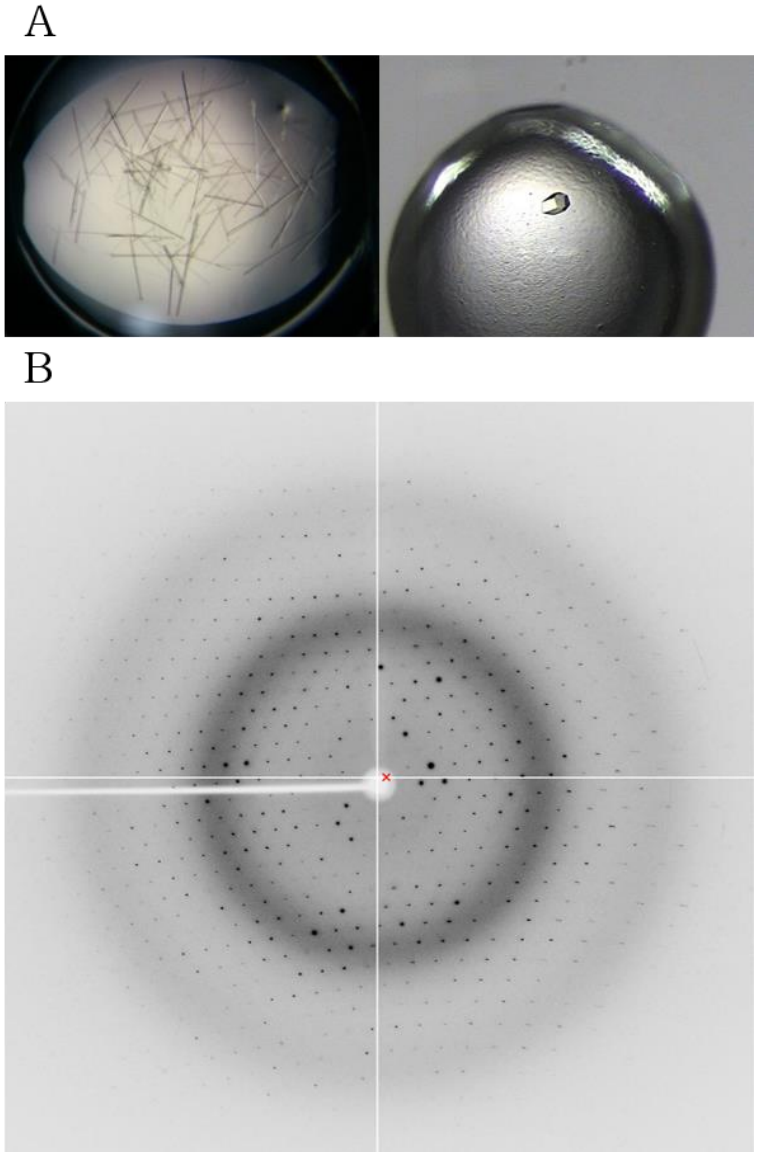

Figure 15. Crystals of UNE-N and their x-ray diffraction. (A) UNE-N crystals grown under the initial screening (left) and a further optimized condition (right). (B) A representative x-ray diffraction image from a UNE-N crystal.

Initial crystals of CD were grown under a commercial crystallization screening condition with 20% (v/v) glycerol, 0.04 M potassium phosphate, and 16% (w/v) PEG 8,000 (Wizard Classic 4, Rigaku, Tokyo, Japan). Initial crystals were further optimized for x-ray diffraction data collection. The crystal was flash-cooled in a nitrogen gas stream at 100 K. Diffraction data were collected at the AR-NW12A beamline of Photon Factory, Japan, and processed at 2.25 Å resolution using the HKL2000 program suite[32]. The structure was solved by molecular replacement using the MOLREP program[36] with the crystal structure of *Bm*NRS (PDB ID: 2XGT)[16] as a phasing model.

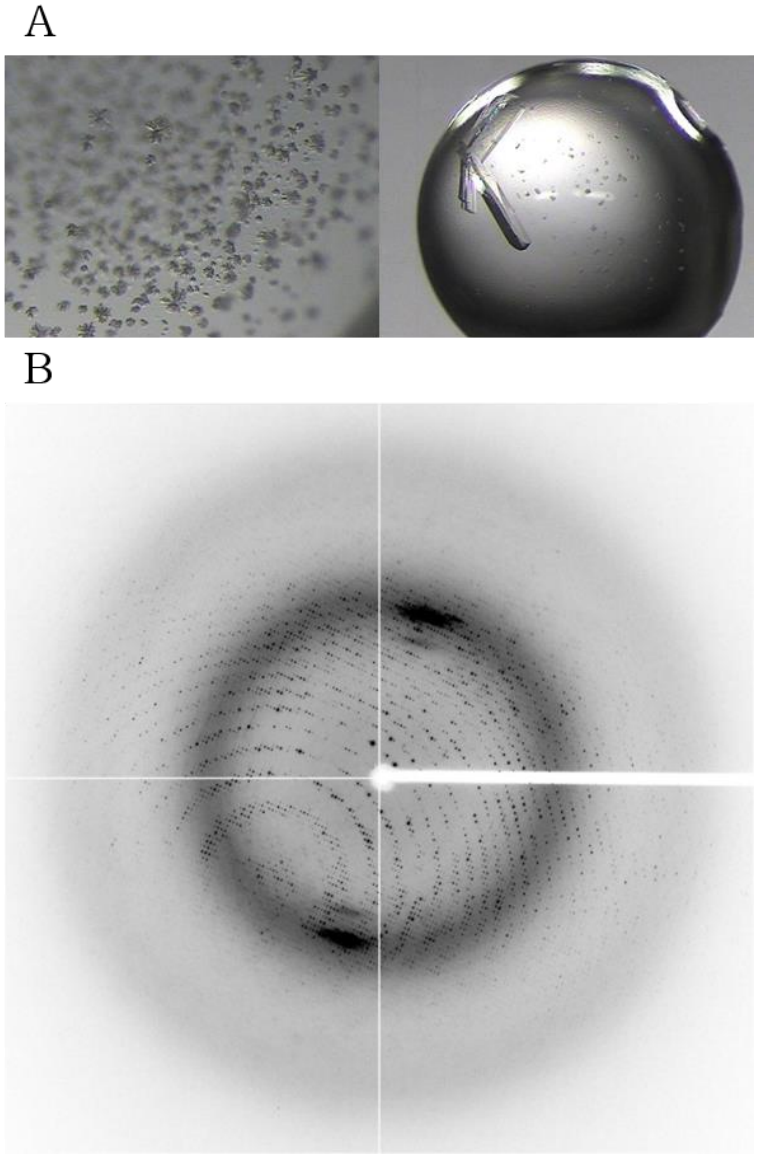

Figure 16. Crystals of CD and their x-ray diffraction. (A) CD crystals grown under the initial screening (left) and a further optimized condition (right). (B) A representative x-ray diffraction image from a CD crystal.

Model building, refinement, and validation for all crystal structures were carried out with the WinCoot program[37], phenix.refine[38], and MOLPROBITY[39], respectively. Statistics for data collection and refinement are summarized in Table 2. The secondary structure of our crystal structures were analyzed with the DSSP program[40,41].

Table 2. Statistics on data collection and refinement.

A. Data collection			
	UNE-N (SAD)	UNE-N	CD
Beamline	PLS-5C	PLS-5C	Photon Factory (AR-NW12A)
Space group	$P6_522$	$P6_5$	$P2_12_12_1$
Unit cell lengths (Å)	32.72, 32.72, 218.86	32.63, 32.63, 215.92	113.35, 127.10, 163.48
Unit cell angles (°)	90, 90, 120	90, 90, 120	90, 90, 90
	Peak		
X-ray wavelength (Å)	0.9796	0.9999	1.0000
Resolution range (Å)	50.00-1.90 (1.93-1.90)[a]	50.00-1.65 (1.68-1.65)[a]	50.00-2.25 (2.29-2.25)[a]
R_{merge}[b]	0.091 (0.401)[a]	0.102 (0.482)[a]	0.099 (0.467)[a]
$\langle I \rangle / \langle \sigma (I) \rangle$	33.2 (12.5)[a]	15.2 (4.1)[a]	19.8 (4.5)[a]
Completeness (%)	99.7 (100.0)[a]	93.7 (94.3)[a]	100.0 (100.0)[a]
Redundancy	35.5 (38.1)[a]	7.1 (6.3)[a]	7.3 (7.1)[a]
B. Model refinement			
PDB code		4ZYA	5XIX
Resolution (Å)		30.00-1.65	30.00-2.25
No. reflections		14,572	112,318
R_{work} / R_{free}[c] (%)		20.8 / 26.0	18.0 / 23.1
No. of non-hydrogen atoms / average B-factor (Å^2)			
Protein		1,184 / 24.26	13,690 / 34.68
Ligand/ion		9 / 28.10	162 / 38.74
Water		135 / 26.73	1,106 / 36.85
R.m.s. deviations from ideal geometry			
Bond lengths (Å)		0.010	0.008
Bond angles (°)		1.130	1.101
Ramachandran[d]			
Favored / Outliers (%)		98.6 / 0.0	97.0 / 0.4
Poor rotamers (%)		0.8	0.8

[a] Values in parentheses refer to the highest resolution shell.

[b] $R_{merge} = \Sigma_h\Sigma_i \mid I(h)_i - \langle I(h) \rangle \mid / \Sigma_h\Sigma_i I(h)_i$, where $I(h)$ is the intensity of reflection h, Σ_h is the sum over all reflections, and Σ_i is the sum over i measurements of reflection h.

[c] $R_{work} = \Sigma \mid \mid F_{obs} \mid - \mid F_{calc} \mid \mid / \Sigma \mid F_{obs} \mid$, where R_{free} is calculated for a randomly chosen 5% of reflections, which were not used for structure refinement and R_{work} is calculated for the remaining reflections.

[d] Values obtained using MolProbity.

2.4. NMR analysis

Uniformly ^{15}N- and ^{13}C-labeled or ^{15}N-labeled UNE-N were prepared by growing the cells in M9 medium, which contained 99% $^{15}NH_4Cl$ and 99% [^{13}C]-D-glucose (Cambridge Isotope Laboratories, Tewksbury, MA, USA). The proteins for three-dimensional (3D), hetero-nuclear nuclear Overhauser effect (NOE), and CLEANEX-PM NMR experiments were prepared at a concentration of approximately 0.6 mM in buffer G with 10% D_2O. For NMR titration experiments with CCR3 EDs, ^{15}N-labeled UNE-N and unlabeled CCR3 EDs were prepared at concentrations of approximately 0.2–0.3 and 0.2–0.6 mM, respectively, in buffer F with 10% D_2O. The NMR experiments were carried out at 298 K on a Bruker AVANCE 800 spectrometer (Billerica, MA, USA) equipped with a cryogenic probe and on a Jeol ECA 600 spectrometer (Tokyo, Japan). Backbone peak assignments of UNE-N were performed using a series of triple resonance spectra [3D HNCO, HN(CA)CO, HNCACB, CBCA(CO)NH]. NMR data were processed with the program NMRPipe[42] and analyzed with the NMRViewJ program (http://www.onemoonscientific.com/ nmrviewj). The overall secondary structure was derived from chemical shifts using the TALOS+ program[43]. (Collaborated with Dr. Ki-Young Lee in

Research Institute of Pharmaceutical Sciences at Seoul National University)

2.5. Cell culture

A549, H460, WI-26, Daudi, Jurkat, and J774A.1 cells were grown in RPMI1640 medium (Hyclone) containing 10% fetal bovine serum and antibiotics (100 UI penicillin and 100 μg/mL streptomycin). DMEM medium containing the same supplements was used for RAW 264.7 culture. Antibodies against NRS, tubulin, and CCR3 were purchased from Abcam (Cambridge, UK), Sigma-Aldrich, and Millipore (Billerica), respectively. (Collaborated with Dr. Min Chul Park, Dr. Peter C. Goughnour, and Dr. Seung Jae Jeong in Medicinal Bioconvergence Research Center at Seoul National University)

2.6. Cell migration assay

Cell migration was determined by using a Transwell plate (5 μm pore size, 24-well, Corning). Cells were seeded in the upper chamber which had been pre-coated with 20 μg/mL fibronectin (BD Biosciences). NRS, UNE-N, and CD were separately added to the lower chamber as attractants and CCL5 as a positive control. After 4 h incubation, cells embedded in the fibronectin coated-membrane were fixed and stained with hematoxylin (Sigma-Aldrich). Non-migrated cells were removed with a cotton swab. The membrane was excised and mounted on slide glass. Migrated cells were monitored by microscopy using a 20X objective lens. (Collaborated with Dr. Min Chul Park, Dr. Peter C. Goughnour, and Dr. Seung Jae Jeong in Medicinal Bioconvergence Research Center at Seoul National University)

2.7. Secretion assay

Cells were seeded and then cultured to 70% confluency. Cells were washed twice with PBS and then incubated under different conditions. Cultured media were harvested and then sequentially centrifuged at 1,000 ×*g* for 10 min and 10,000 ×*g* for 20 min to remove cells and debris, respectively. To precipitate proteins, trichloroacetic acid (TCA) (Sigma-Aldrich) was added to a 10% final concentration. After 12 h incubation, secreted proteins were pelleted by 20,000 ×*g* centrifugation. Precipitated proteins were resuspended in 100 mM HEPES (pH 8.0) and then separated by SDS-PAGE for immunoblotting. (Collaborated with Dr. Min Chul Park, Dr. Peter C. Goughnour, and Dr. Seung Jae Jeong in Medicinal Bioconvergence Research Center at Seoul National University)

2.8. Immunoblotting

Cells were lysed on ice by M-PER mammalian protein extraction reagent (Pierce Biotechnology). After removing cell debris by centrifugation, protein concentration was measured using Bradford solution (Bio-Rad). Proteins were separated by SDS-PAGE and then transferred to polyvinylidene fluoride membrane for immunoblotting with specific antibodies. (Collaborated with Dr. Min Chul Park, Dr. Peter C. Goughnour, and Dr. Seung Jae Jeong in Medicinal Bioconvergence Research Center at Seoul National University)

2.9. Pull-down assay

Four MBP-fused CCR3 EDs were incubated with NRS, UNE-N, CD, or CCL5 in PBS containing 5% glycerol, respectively. After 2 h incubation, amylose-resin (New England Biolabs) was added to pull down MBP-fused proteins. Precipitated proteins were resolved by SDS-PAGE. Co-precipitated proteins with MBP-fused CCR3 EDs were detected by Coomassie blue staining (Expedeon). (Collaborated with Dr. Min Chul Park, Dr. Peter C. Goughnour, and Dr. Seung Jae Jeong in Medicinal Bioconvergence Research Center at Seoul National University)

2.10. Statistical analysis

Statistical analysis was performed using Dunnett's multiple comparison test and two-tailed Student's *t*-test. All graphs are presented as the mean ± standard deviation. Differences were considered statistically significant at a P value < 0.05. (Collaborated with Prof. Jae-Young Lee in College of Pharmacy at Chungnam National University)

2.11. Data deposition

The coordinates and structure factors of UNE-N and CD have been deposited in the Protein Data Bank (http://www.rcsb.org) under ID codes 4ZYA and 5XIX, respectively.

3. Results

3.1. UNE-N shares a structural scaffold with the chemotactic N-terminal domain of *Bm*NRS but exhibits unique features

Human NRS is composed of a UNE-N, an ABD, an HR, and a catalytic domain. I determined the crystal structures of UNE-N (residues 4-77) and CD (residues 98-548) of NRS at 1.65 and 2.25 Å resolution, respectively (Fig. 17). UNE-N is composed of two α-helices (α1, α2) and three β-strands (β1, β2, β3) with β1-α1-β2-β3-α2 topology. Three β-strands form a parallel/antiparallel mixed β-sheet (Fig. 18A). DALI server analysis for structural similarity searching with known protein structures predicted that the most similar structure to UNE-N is the UNE-N of *B. malayi* (PDB ID: 2KQR) with a Z-score of 7.3 and 27% amino acid sequence identity[44]. Despite the low sequence identity, superposition of the UNE-N structures of human and *B. malayi* showed that the overall folds are very similar with a root-mean-square deviation (RMSD) of 2.3 Å for all C_α atoms (Fig. 18B). The overall structural similarity of UNE-Ns initially indicated

that the human UNE-N domain also plays a chemokine-like role like UNE-N of *B. malayi*.

The lysine-rich helical motif, iSKsqLKnikK, was also observed at the N-terminus of helix $\alpha 2$, which implies interactions with its substrate tRNAs as shown in UNE-N of *B. malayi*[16] (Fig. 18C).

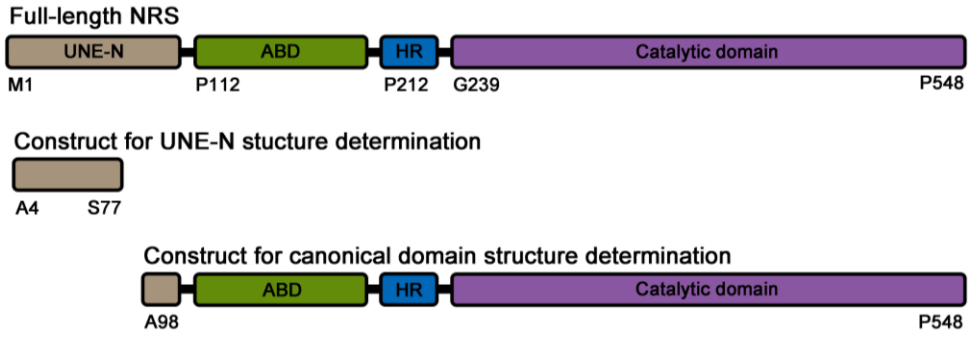

Figure 17. Domain composition of NRS. UNE-N, ABD, and HR indicate N-terminal extension domain, anticodon-binding domain, and hinge region, respectively. Three NRS constructs with full-length (residue 1-548), UNE-N (residue 4-77), and CD (residue 98-548) were used for structure determination and biological experiments.

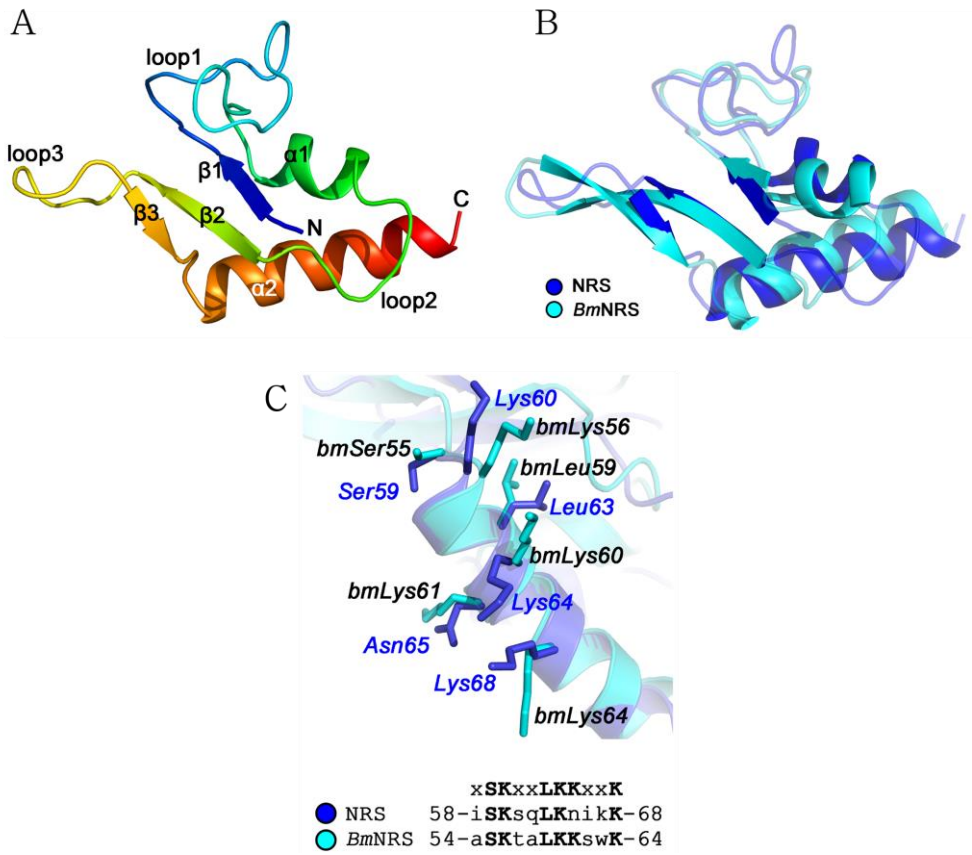

Figure 18. Crystal structure of UNE-N. (A) Crystal structure of UNE-N shown in rainbow cartoon representation depicting amino acid residues from N-terminus to C-terminus in blue to red. (B) Secondary-structure match superposition of UNE-Ns of human and *B. malayi* (PDB ID: 2KQR). UNE-Ns of human and *B. malayi* are displayed in cartoon representation colored in blue and cyan, respectively. (C) Lysine-rich motifs of UNE-Ns of human and *B. malayi* are superposed with respect to the main chain of helix α2. Amino acid sequences of each lysine-rich motif are shown below.

Interestingly, the β2-loop3-β3 region exhibits remarkable structural differences. UNE-N has longer loop3 with Ser48-Arg54 residues and shorter β-strands in both ends of loop3 (β2 and β3), while UNE-N of *B. malayi* contains a β-hairpin structure with a type Ⅱ β-turn (Lys45-Asp46-Gly47-Lys48) and longer β-strands. NMR studies on UNE-N showed consistent results for the secondary structure propensity of loop3 with the crystal structure (Table 3).

In UNE-N of *B. malayi*, the β-hairpin structure that is equivalent to loop3 of human UNE-N was suggested as a minimal motif for the interaction with CXCR1/2[22]. Loop3 of human UNE-N also seemed as the region for the receptor specificity to CCR3, and thus for subsequent CCR3-mediated signal transduction, which is further discussed below.

Table 3. NMR chemical shift-based prediction for the secondary structure of UNE-N using the TALOS+ program.

Residue	Secondary structure	Confidence level
3 L	L	0.76
4 A	L	0.76
5 E	L (E)	0.19
6 L	E	0.69
7 Y	E	0.81
8 V	E	0.56
9 S	L	0.19
10 D	L	0.52
11 R	L	0.31
12 E	L	0.65
13 G	L	0.93
14 S	L	0.84
15 D	L	0.66
16 A	L	0.8
17 T	L	0.92
18 G	L	0.97
19 D	L	0.96
20 G	L	0.96
21 T	L	0.87
22 K	L	0.57
23 E	L	0.51
24 K	L	0.79
25 P	L	0.9
26 F	L	0.87
27 K	L	0.85
28 T	L	0.81
29 G	L (H)	0.84
30 L	H	0.62
31 K	H	0.91
32 A	H	0.9
33 L	H	0.87
34 M	H	0.83
35 T	H	0.74
36 V	H (L)	0.35
37 G	L	0.5
38 K	L	0.91
39 E	L	0.94
40 P	L	0.86
41 F	L	0.93

42 P	L	0.93
43 T	L (E)	0.81
44 I	E	0.26
45 Y	E	0.65
46 V	L (E)	0.28
47 D	L (E)	0.85
48 S	L	0.8
49 Q	L	0.89
50 K	L	0.89
51 E	L	0.88
52 N	L	0.87
53 E	L	0.89
54 R	L	0.79
55 W	E	0.17
56 N	E	0.59
57 V	E	0.2
58 I	L	0.43
59 S	L (H)	0.72
60 K	H	0.66
61 S	H	0.94
62 Q	H	0.96
63 L	H	0.97
64 K	H	0.96
65 N	H	0.96
66 I	H	0.98
67 K	H	0.98
68 K	H	0.97
69 M	H	0.95
70 W	H	0.93
71 H	H	0.87
72 R	H	0.63
73 E	H	0.32
74 Q	L (H)	0.14
75 M	L (H)	0.53
76 K	L	0.57

Note: H, E, and L in the secondary structure column represent α-helix, β-strand, and loop, respectively. The secondary-structure elements in parenthesis are derived from the crystal structure of UNE-N.

In addition, the loop3 region was the most dynamic part in UNE-N from the $^{1}H-^{15}N$ hetero-nuclear NOE experiment (Fig. 19) and the amide proton exchange rates for the loop3 region and the N-terminus of helix $\alpha 2$ were higher than those for the other parts (Fig. 20 and Fig. 21), which further supports the dynamic nature of the loop3 region.

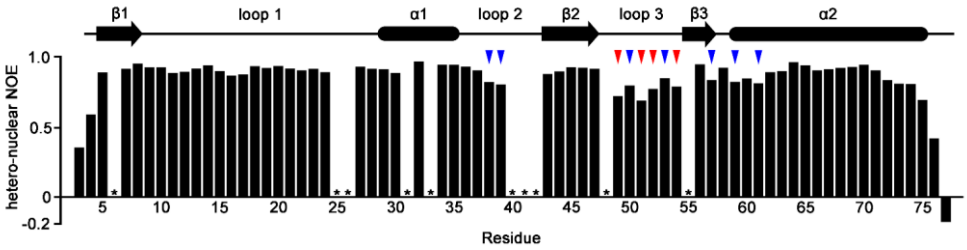

Figure 19. Hetero-nuclear $^{1}H-^{15}N$ NOE data of UNE-N. Hetero-nuclear NOE values are plotted against UNE-N residues. Residues showing the lowest and second-lowest NOE values are indicated by red and blue down arrows, respectively (red arrows: hetero-nuclear NOE value < 0.8, blue arrows: 0.8 < hetero-nuclear NOE value < 0.85). N-terminal and C-terminal residues are excluded for potential fast motions. The spectra were recorded at 298 K in a buffer containing 150 mM NaCl, 20 mM NaH_2PO_4/Na_2HPO_4 (pH 6.5), and 10% D_2O. The residues showing unclear peaks because of overlaps or inadequate signal to noise (S/N) were omitted and are denoted by * marks.

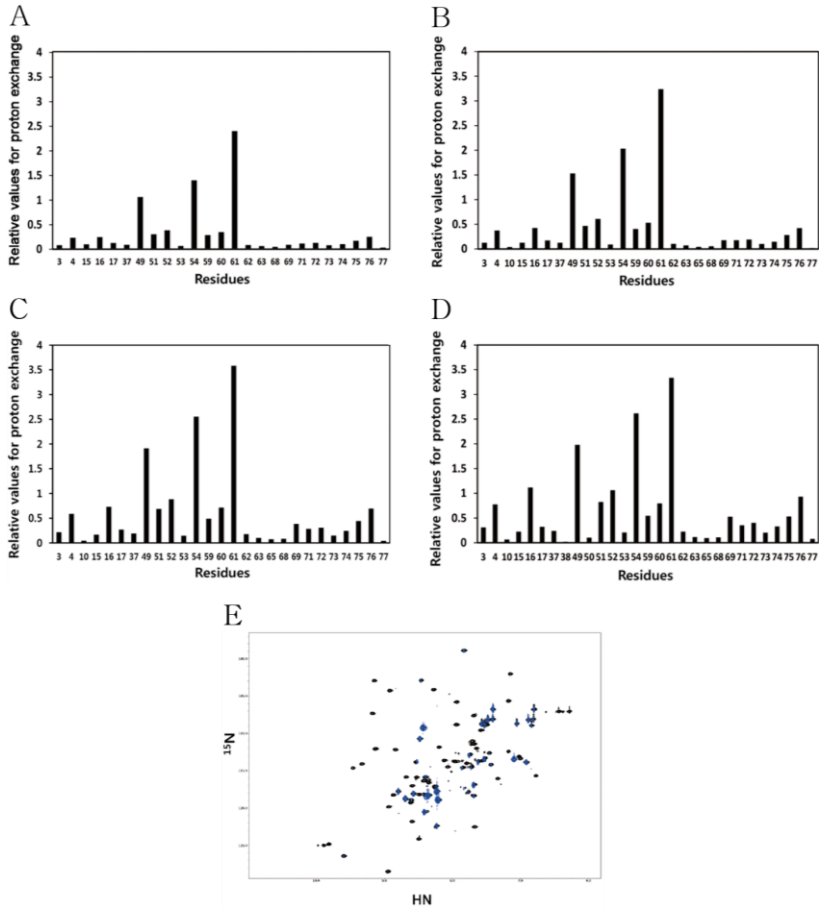

Figure 20. Dynamics of UNE-N obtained from CLEANEX-PM spectra. (A-D) Relative peak intensities measured from CLEANEX-PM spectra of UNE-N are plotted against residues number. The data were acquired at various proton-exchange mixing times of 20 (A), 50 (B), 100 (C), and 200 ms (D), respectively. (E) Overlay of conventional $^{1}H-^{15}N$ HSQC and representative CLEANEX-PM spectrum (200 ms) of UNE-N. The two spectra are colored in black and blue, respectively. All spectra were recorded at 298 K in a buffer containing 150 mM NaCl, 20 mM NaH_2PO_4/Na_2HPO_4 (pH 6.5), and 10% D_2O.

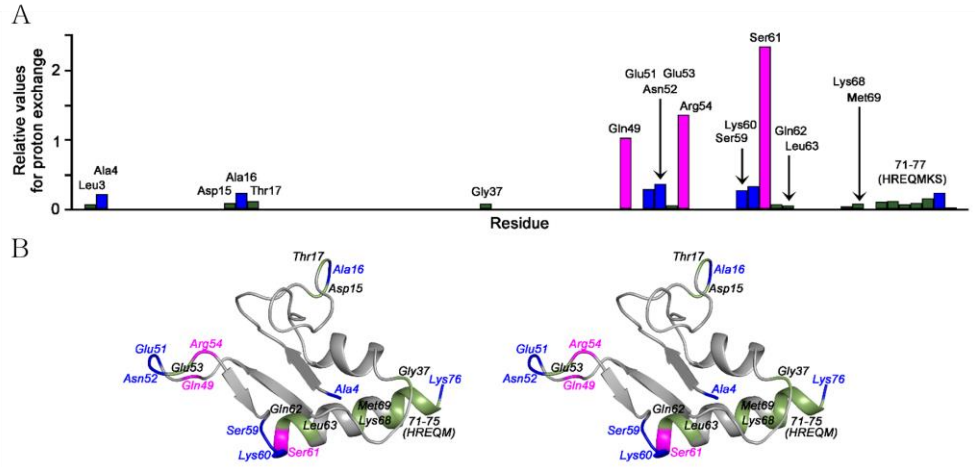

Figure 21. CLEANEX-PM spectrum represented on crystal structure of UNE-N. (A) Plot of peak intensities on the CLEANEX-PM spectrum of UNE-N against residue number. Residues with relative values of proton exchange higher than 1, between 0.1 and 1, and lower than 0.1 are colored in magenta, blue, and green, respectively. The spectrum was obtained with a proton-exchange mixing time of 20 ms and recorded at 298 K in a buffer containing 150 mM NaCl, 20 mM NaH_2PO_4/Na_2HPO_4 (pH 6.5), and 10% D_2O. (B) A stereo-view image of UNE-N on which residues are mapped and colored as in (A).

When I compared $^{1}H-^{15}N$ HSQC spectrum of UNE-N including further C-terminal residues (UNE-N_{111}, residues 1-111) with the spectrum of UNE-N (Fig. 22), most peaks for residual residues 78-111 of UNE-N_{111} clustered around 8.2 ppm, indicating that the residual region adopts an unfolded state and does not affect the structure of UNE-N.

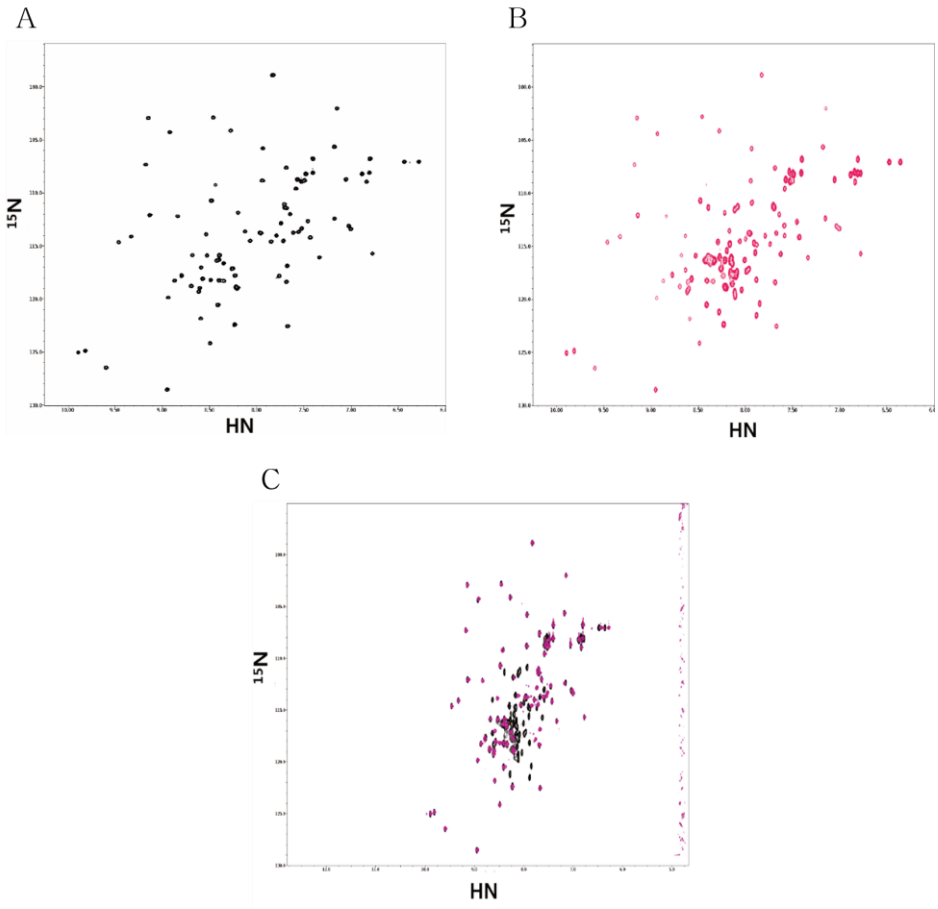

Figure 22. Comparison of $^{1}H-^{15}N$ HSQC spectra of UNE-N and UNE-N_{111}. (A) $^{1}H-^{15}N$ HSQC spectrum of UNE-N (residues 1-77). (B) $^{1}H-^{15}N$ HSQC spectrum of UNE-N_{111} (residues 1-111). (C) Overlay of the spectra of UNE-N (black) and UNE-N_{111} (magenta). Most peaks for residual residues 78-111 of UNE-N_{111} clustered around 8.2 ppm. All spectra were recorded at 298 K in a buffer containing 150 mM NaCl, 20 mM NaH_2PO_4/Na_2HPO_4 (pH 6.5), and 10% D_2O.

I also determined the crystal structure of CD of NRS using the molecular replacement method with the crystal structure of *Bm*NRS (Fig. 23). CD shares considerable structural similarities with NRSs from *B. malayi*, *Pyrococcus horikoshii*, and *Entamoeba histolytica*, as calculated by the DALI server[44]. The catalytic domain of CD features a nucleotide-binding site with an antiparallel β-sheet flanked with α-helices, which is a structural characteristic of the class 2 ARS family. The dimeric interface of CD is widely spread through ABD and the catalytic domain of 3,800 $Å^2$, which covers approximately 18% of the monomeric surface area of CD, as calculated using the PISA (Protein interfaces, surfaces, and assemblies) server[45].

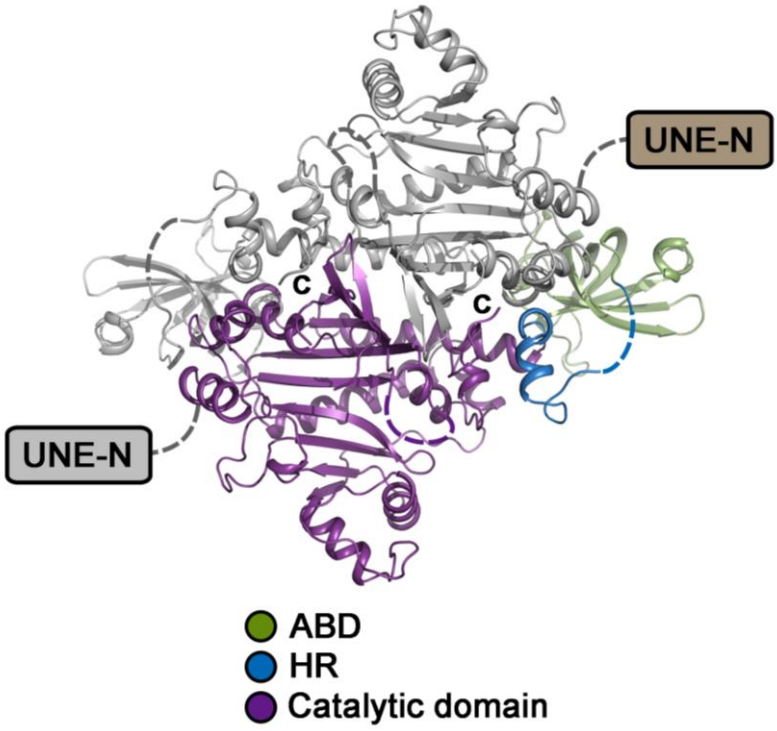

Figure 23. Crystal structure of CD. ABD, HR, and catalytic domain are colored in green, blue, and purple, respectively. The homodimeric pair is colored in gray.

3.2. Th1 and Th2 cytokines induce NRS secretion from macrophages

Autoantibodies against NRS have been detected in the sera of ILD patients and most cytokine-like ARSs are secreted from immune cells[46,47]. Therefore, NRS secretion levels in seven different cell lines were measured. Seven cell lines (A549, H460, WI-26, Daudi, Jurkat, RAW 264.7, and J774A.1) were incubated in serum-free medium for 12 h and proteins secreted into the medium were precipitated by TCA. The precipitated proteins were separated and the presence of NRS was determined by western blot analysis with an NRS-specific antibody. Among the seven tested cell lines, NRS was detected in the culture media obtained from macrophage cell lines, RAW 264.7 and J774A.1 (Fig. 24). Under the same conditions, release of tubulin into the medium was not observed, confirming that NRS in the culture medium was not caused by cell lysis. These results showed that NRS is constitutively secreted from macrophages.

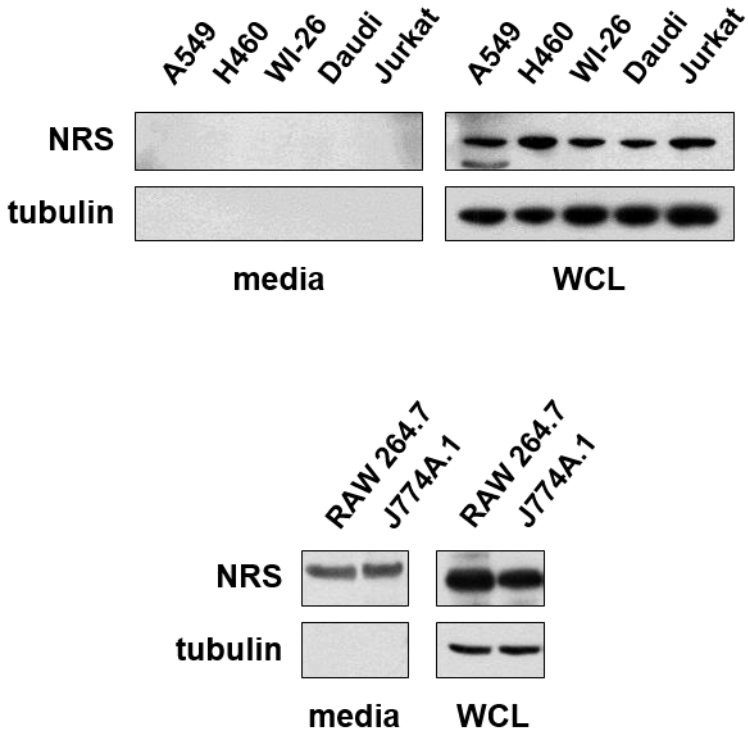

Figure 24. Secretion of NRS from macrophages. Seven cell lines were tested for NRS secretion. A549, adenocarcinomic human alveolar basal epithelial cell line; H460, human lung cancer cell line (NCI-H460); WI-26, human diploid lung fibroblast cell line; Daudi, human B lymphoblast cell line; Jurkat, human T lymphocyte cell line; RAW 264.7, mouse macrophage cell line; J774A.1, mouse monocyte/macrophage cell line. Secreted NRS was determined by western blotting after 12 h culture in serum-free media.

To further determine whether NRS secretion is influenced by other stimuli, RAW 264.7 and J774A.1 cells were treated with three representative cytokines, tumor necrosis factor (TNF)-α, interferon (IFN)-γ, and transforming growth factor (TGF)-β. TNF-α and IFN-γ influence Th1 differentiation and TGF-β regulates Th2 differentiation. All three cytokines increased NRS secretion from the macrophage cells (Fig. 25), indicating that increased NRS secretion by cytokines plays an active role in Th1 and Th2 responses, resulting in immune cell recruitment.

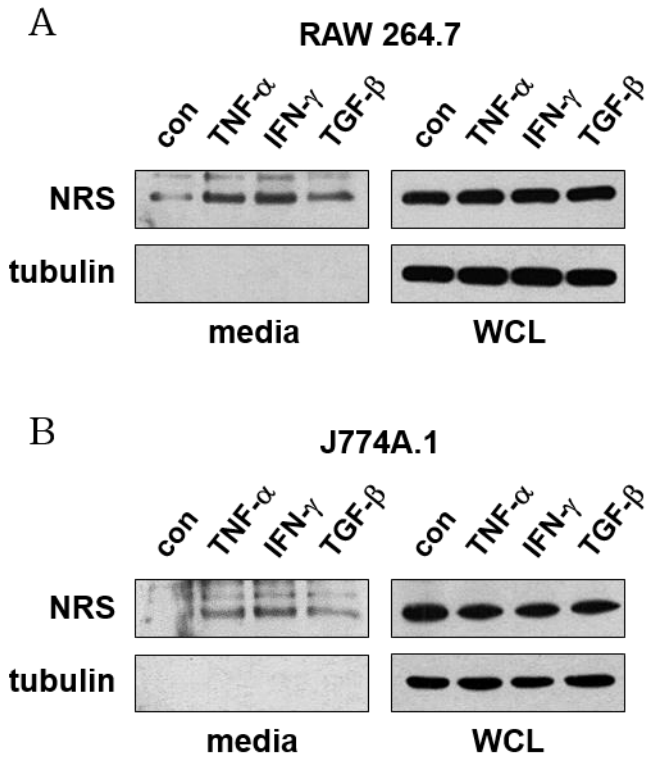

Figure 25. Induction of NRS secretion by cytokines. RAW 264.7 (A) and J774A.1 (B) cells were incubated with three cytokines, TNF-α (10 ng/mL), IFN-γ (150 U/mL), and TGF-β (20 ng/mL) for 4 h. Secreted proteins were precipitated by TCA solution and detected by immunoblotting.

3.3. UNE-N exclusively elicits chemotactic activities of NRS on Daudi and Jurkat cells

To narrow down the functional determinants of NRS for the chemokine activities on lymphocytes, iDCs, and CCR3-transfected HEK293 cells[18,19] and to examine whether the evolutionarily acquired UNE-N plays a role in the chemokine activity of NRS, cell migration assays were conducted with three different constructs, NRS, UNE-N (residues 1-77), and CD (residues 98-548). Daudi, Jurkat, and H460 cell lines were used as representative B cells, T cells, and cancer cells, respectively, and seeded into the upper chamber coated with fibronectin. Then, the lower chamber media were treated with NRS, UNE-N, and CD at 0.1, 1, and 10 nM. Microscopic analysis showed that NRS and UNE-N induced the migration of Daudi and Jurkat cells, while CD did not affect the migration of any cells. No migration effect was observed for H460 cells, further supporting that the chemokine activity of NRS specifically targets the immune cells (Fig. 26).

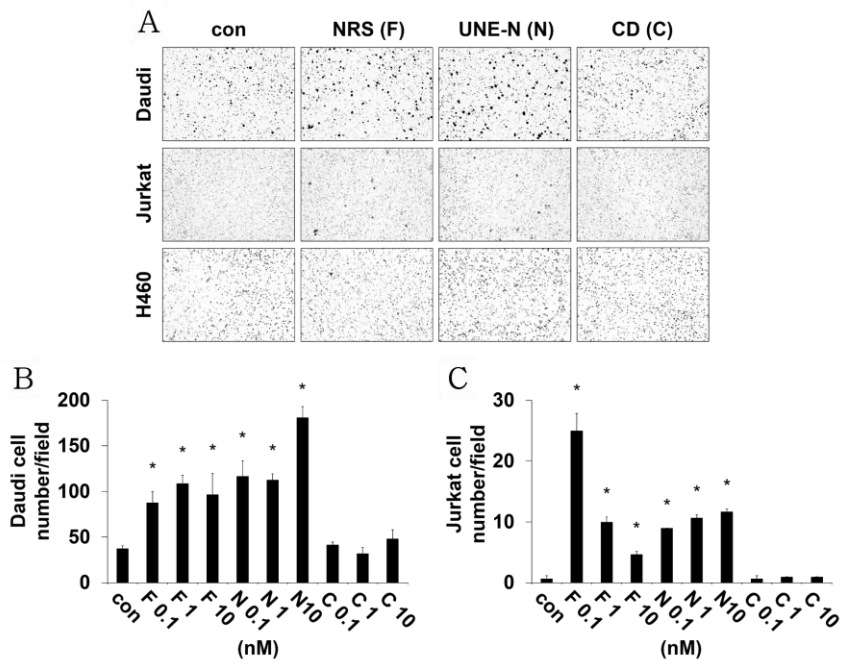

Figure 26. Chemokine activity of UNE-N. (A) Cell migration induced by NRS. Daudi, Jurkat, and H460 cells were seeded in the fibronectin-coated upper chamber of a Transwell and NRS, UNE-N, and CD were added to the lower chamber at 1 nM. After 4 h incubation, fibronectin-coated membranes were harvested. Migrated cells embedded in the harvested membrane were stained and then monitored by microscopy. (B,C) Cell migrations induced by various concentrations of NRS. Migration of Daudi (B) and Jurkat (C) cells was quantified by cell counting. Labels on the X-axis represent NRS construct and concentration: F, full-length NRS; N, UNE-N; C, CD. Error bars indicate the mean ± standard deviation from the average of three independent experiments. Significant differences were determined by Dunnett's multiple comparison test. $*P < 0.05$.

When NRS was added to both the upper chamber and the lower chamber, the migration of Jurkat cells was blocked, which shows that NRS induced chemotaxis rather than chemokinesis (Fig. 27). Collectively, the data reveal that the evolutionally acquired UNE-N is the functional motif necessary and sufficient for inducing the migration of Daudi and Jurkat cells.

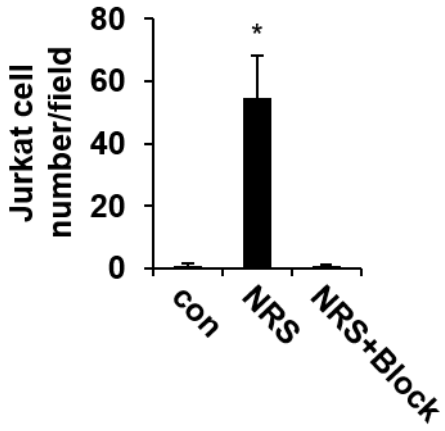

Figure 27. NRS induces chemotaxis, not chemokinesis. The migration of Jurkat cells was blocked when 1 nM of NRS was added to both the upper chamber and the lower chamber of a Transwell. Error bars indicate the mean ± standard deviation from the average of three independent experiments. Significant differences were determined by Dunnett's multiple comparison test. $*P < 0.05$.

3.4. UNE-N directly interacts with CCR3 extracellular domains

To further elucidate whether UNE-N exerts its chemokine activity via CCR3, the migration of Daudi and Jurkat cells by UNE-N was tested when CCR3 expression was suppressed by a specific CCR3-targeting siRNA (si-CCR3) (Fig. 28A-C). The chemokine activities of NRS and UNE-N were significantly reduced as CCL5, a well-established chemokine of CCR3[30], which was used as a positive control (Fig. 28D,E). These results indicate that UNE-N elicits its chemokine activity via CCR3 as a possible functional receptor.

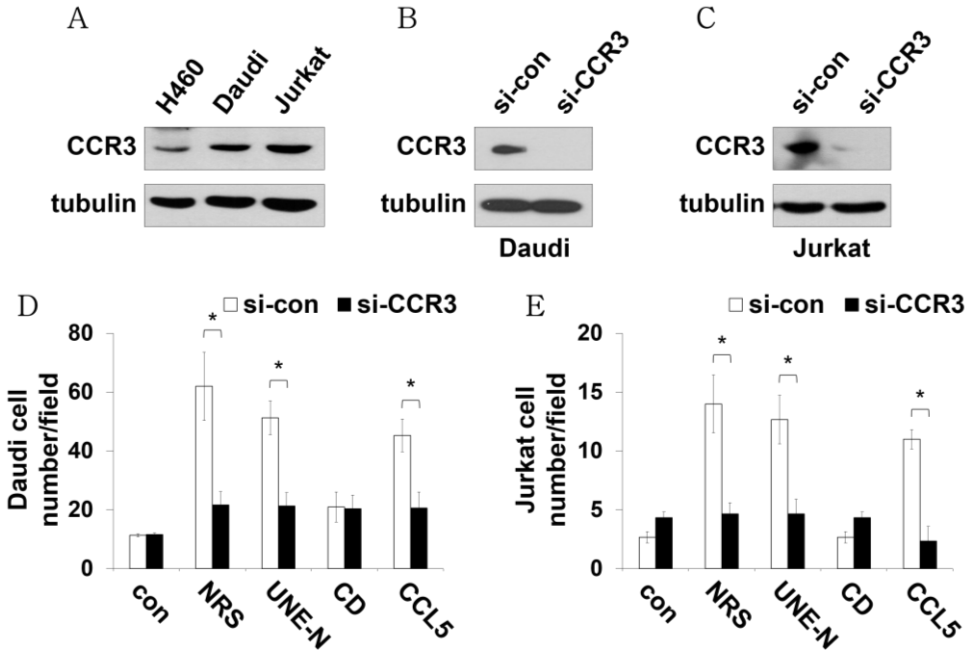

Figure 28. CCR3 mediates chemokine activity of NRS. (A) CCR3 expression in H460, Daudi, and Jurkat cells was determined by immunoblotting. (B,C) Confirmation of CCR3 knock-down by si-CCR3. CCR3 expression in Daudi (B) and Jurkat (C) cells after si-CCR3 treatment was determined by immunoblotting. (D,E) Effects of CCR3 knock-down on NRS-induced cell migration of Daudi (D) and Jurkat (E) cells. The cells down-regulated by CCR3-targeting siRNA (si-CCR3) were used for the migration assay. Error bars indicate the mean ± standard deviation from the average of three independent experiments. Significant differences were determined by Student's *t*-test. $*P < 0.05$.

Next, to narrow down the binding propensities of UNE-N with respect to CCR3 EDs, the *in vitro* interaction between NRS and CCR3 EDs was evaluated. CCR3 ED1, ED2, ED3, and ED4 with a MBP tag at each N-terminus were purified and incubated with NRS, UNE-N, CD, or CCL5. MBP control without CCR3 EDs did not pull down NRS, UNE-N, CD, and CCL5. Interestingly, NRS and UNE-N were co-precipitated with CCR3 EDs, while CD and CCL5 were not pulled down (Fig. 29). Particularly, CCR3 ED3 bound more strongly to NRS/UNE-N than CCR3 ED1 and ED2 did and a weak interaction between CCR3 ED4 and NRS/UNE-N was observed. CCL5 was not co-precipitated with CCR3 EDs, which needs further attention regarding to the condition of *in vitro* interaction between CCL5 and CCR3 EDs as will be discussed below. These results indicate that UNE-N exerts CCR3-mediated chemokine activity and directly binds to CCR3 ED3, ED2/ED1, and ED4 in a descending order of affinity.

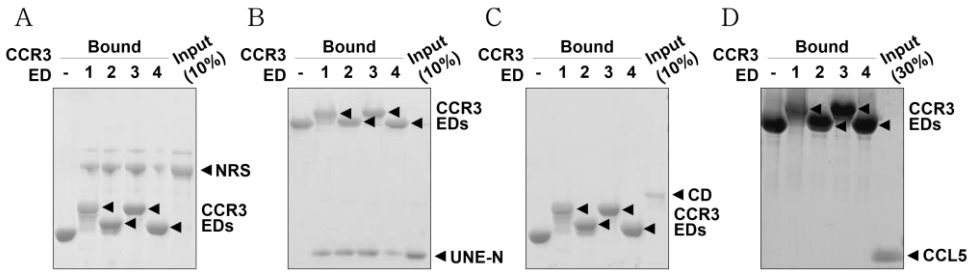

Figure 29. Direct interaction of UNE-N with CCR3. (A-D) Interaction between NRS and CCR3 EDs. For *in vitro* binding assay, MBP without CCR3 EDs (as a control, lane '-') and four MBP-fused CCR3 EDs (ED1-ED4, lanes 1-4) were separately incubated with NRS (A), UNE-N (B), CD (C), and CCL5 (D), and then precipitated by maltose resin. Co-precipitated proteins were resolved by SDS-PAGE and detected by Coomassie blue staining.

3.5. Loop3 of UNE-N is an effector motif for CCR3 interactions

To further investigate the binding mode of UNE-N to CCR3, $^{1}H-^{15}N$ HSQC spectra of UNE-N were measured in the absence and presence of four individual CCR3 EDs. It showed that CCR3 ED3 caused the most perturbed spectra peaks with predominant resonance broadenings rather than chemical shift perturbations. Overall resonance broadenings can be explained by the remarkable increases in transverse relaxation rates (R2) of UNE-N when it bound to MBP-fused CCR3 EDs. Similar peak changes were observed in the spectra of UNE-N titrated with CCR3 ED1 to a lesser extent. CCR3 ED2 caused slight resonance broadenings without chemical shift changes and CCR3 ED4 did not cause noticeable spectral changes. These results indicate that the binding preference for UNE-N is CCR3 ED3, ED1, ED2, and ED4, in a descending order, which is consistent with the pull-down assay results in that UNE-N binds most strongly to CCR3 ED3.

The degrees of resonance broadenings may be derived from the ratios of peak intensities of the spectra in the absence and presence of CCR3 EDs. When these values elicited by CCR3 ED3, ED1, and ED2 were plotted with respect to UNE-N residues, the average ratio/standard deviation for each plot was 0.530/0.066 (ED3), 0.575/0.052 (ED1), and 0.794/0.056 (ED2), respectively (Fig. 30). Larger standard deviation values for UNE-N residues can be interpreted as UNE-N residues are more specifically affected by CCR3 binding and residue-by-residue analysis of UNE-N would reveal the binding mode more in detail.

To identify the interacting residues of UNE-N with each CCR3 ED, the resonance broadenings and chemical shift perturbations were quantified. In the presence of CCR3 ED3, Glu51 and Asn52 in loop3 and Lys60 in helix $\alpha 2$ showed the largest resonance broadenings (Fig. 30A).

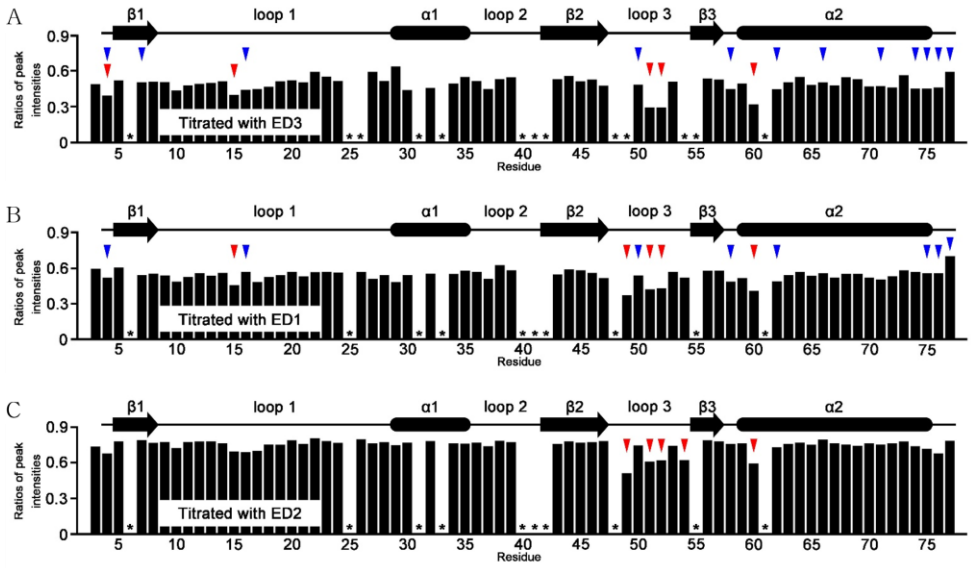

Figure 30. Key residues of UNE-N involved in the interaction with CCR3. (A-C) Ratios of peak intensities are plotted against UNE-N residues in the presence of CCR3 ED3 (A), ED1 (B), and ED2 (C), each of which is fused to MBP. The molar ratio of UNE-N to MBP-fused CCR3 EDs used was approximately 1:1. Residues showing large resonance broadenings (ratio < 0.85) and chemical shift perturbations are marked with red and blue down arrows, respectively. All titration experiments were carried out at 298 K in a buffer containing 150 mM NaCl, 20 mM NaH_2PO_4/Na_2HPO_4 (pH 7.5), and 10% D_2O. Residues showing unclear peaks because of overlaps or inadequate signal to noise (S/N) were omitted and are denoted by * marks.

Considering that the conformational change on the intermediate NMR time scale increases resonance broadening of corresponding peaks, loop3 (Glu51 and Asn52) and the N-terminus of helix $\alpha 2$ (Lys60) undergo the most remarkable conformational changes when UNE-N interacts with CCR3 ED3. Slight chemical shift perturbations upon binding to CCR3 ED3 were observed for Ala4, Tyr7, Ala16, Lys50, Ile58, Gln62, Ile66, His71, Gln74, Met75, Lys76, and Ser77 (Fig. 31), suggesting slight structural changes on the fast NMR time scale.

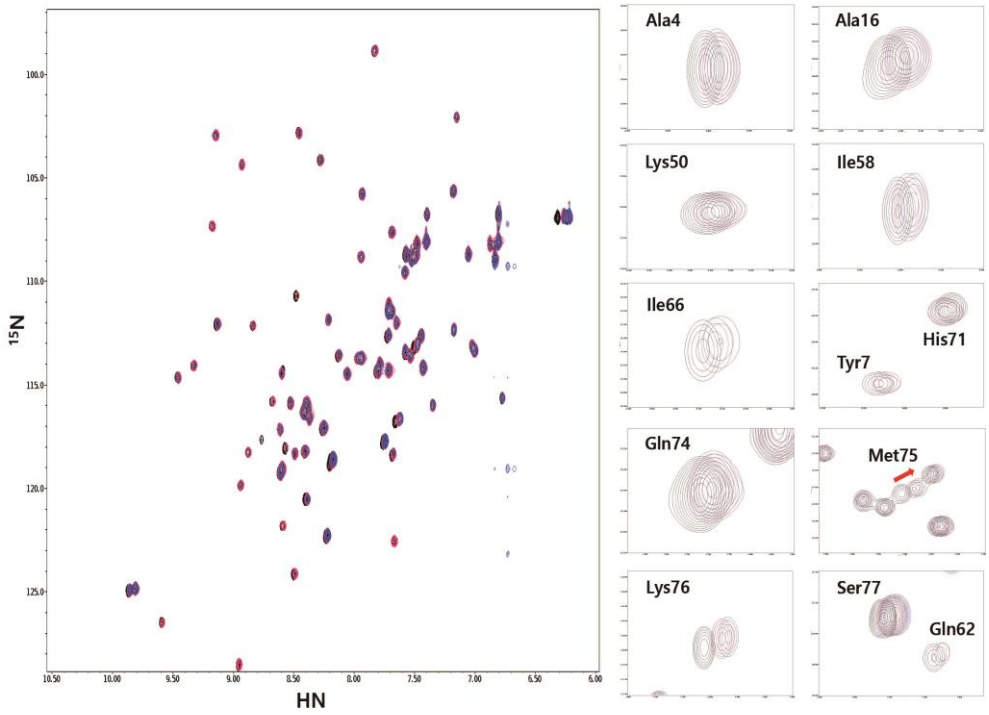

Figure 31. Chemical shift perturbations of UNE-N upon binding to CCR3 ED3. Expanded views of 12 residue peaks with relatively large chemical shift changes are shown on the right-hand side. The molar ratios of UNE-N/MBP-fused CCR3 ED3 were approximately 1:0, 1:1, and 1:2, which are color-mapped onto peaks in black, red, and blue, respectively. All 2D $^{1}H-^{15}N$ HSQC spectra were recorded at 298 K in a buffer containing 150 mM NaCl, 20 mM NaH_2PO_4/Na_2HPO_4 (pH 7.5), and 10% D_2O.

Following titration with CCR3 ED1, Gln49 in loop3 showed the largest resonance broadening, while Glu51, Asn52, and Lys60 showed the second largest broadening (Fig. 30B), supporting that loop3 of UNE-N is mainly involved in binding to CCR3 ED1. Chemical shift perturbations upon binding to CCR3 ED1 were observed for Ala4, Ala16, Lys50, Ile58, Met75, Lys76, and Ser77, with lower values than those caused by CCR3 ED3 (Fig. 32). Similar to the titration with CCR3 ED1, Gln49 in loop3 elicited the largest resonance broadening and Glu51, Asn52, Arg54, and Lys60 caused the second largest in the presence of CCR3 ED2 (Fig. 30C). Collectively, these results suggest that loop3 in UNE-N plays a major role in binding to CCR3 and is an effector motif for the receptor recognition of UNE-N.

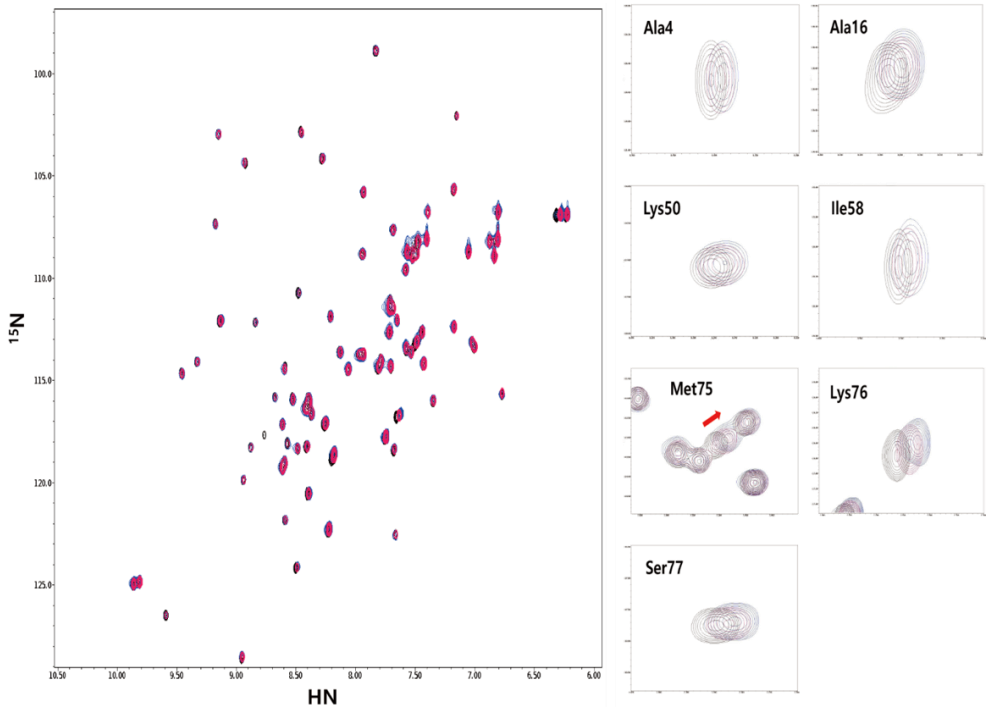

Figure 32. Chemical shift perturbations of UNE-N upon binding to CCR3 ED1. Expanded views of seven residue peaks with relatively large chemical shift changes are shown on the right-hand side. The molar ratios of UNE-N/MBP-fused CCR3 ED1 were approximately 1:0, 1:1, and 1:2, which are color-mapped onto peaks in black, red, and blue, respectively. All 2D $^{1}H-^{15}N$ HSQC spectra were recorded at 298 K in a buffer containing 150 mM NaCl, 20 mM NaH_2PO_4/Na_2HPO_4 (pH 7.5), and 10% D_2O.

3.6. Loop3 region of UNE-N is structurally distinct from UNE-N of *Bm*NRS targeting different receptors

To gain insights into the structural contribution of loop3 of UNE-N in target receptor selection, nine UNE-N sequences from representative eukaryotes were aligned; human, monkey, mouse, bird, frog, fish, insect, and two nematodes (Fig. 33). Two aromatic amino acid residues near loop3, Tyr7 and Trp55, are highly conserved among various NRSs. Comparison of the structures of UNE-Ns from human and *B. malayi* revealed that the secondary structure composition of loop3 region was notably different, although the overall structures were similar and some characteristic residues near loop3 region are highly conserved.

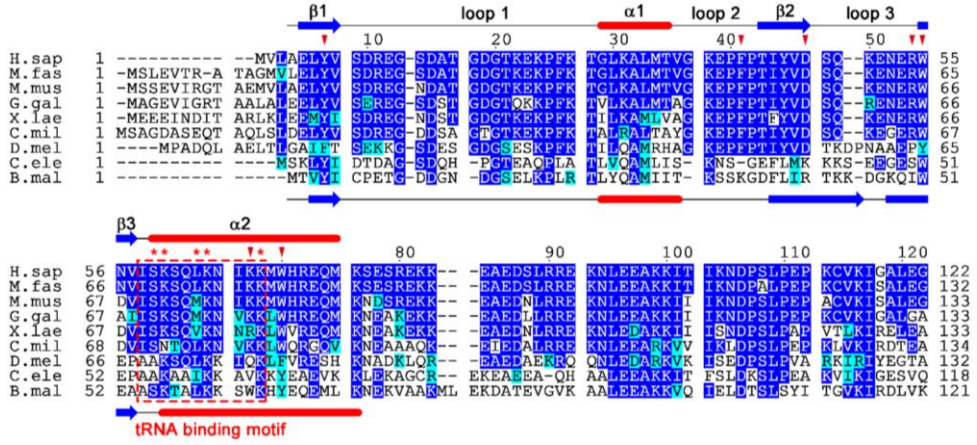

Figure 33. Sequence alignment of UNE-Ns from nine eukaryotic NRSs: H.sap, *Homo sapiens*; M.fas, *Macaca fascicularis*; M.mus, *Mus musculus*; G.gal, *Gallus gallus*; X.lae, *Xenopus laevis*; C.mil, *Callorhinchus milii*; D.mel, *Drosophila melanogaster*; C.ele, *Caenorhabditis elegans*; B.mal, *Brugia malayi*. Residues identical or conserved in UNE-Ns are colored in blue or cyan, respectively. Secondary structure elements of NRS and *Bm*NRS are represented above and below the sequences with red tube for α-helix and blue arrow for β-strand, respectively. Representative residues of conformational importance are denoted with red down arrows. The red dashed box and asterisks denote the conserved tRNA-binding motif.

The aromatic side chains of Tyr7 and Trp55 of NRS interact with each other via a pi-pi interaction, stabilizing protein folding. On the opposite side of the Typ7-Trp55 interface, the side chain of Arg54, which is conserved in vertebrates, also stabilized Trp55 via a cation-pi interaction according to the CaPTURE web server calculations[48]. Additionally, the negatively charged carboxyl group of Asp47, which is conserved in vertebrates, stabilized the positively charged guanidinium group of Arg54 electrostatically. For UNE-N of *Bm*NRS, Tyr4 and Trp51 correspond to Tyr7 and Trp55 of human NRS, respectively, and form a pi-pi interaction through aromatic side chains of Tyr-Trp. However, *Bm*NRS lacks the basic residue corresponding to Arg54 of human NRS, but the positively charged guanidinium group of Arg42 (equivalent to Asp47 of human NRS) alternatively occupies the Arg54 site of human NRS and interacts with Trp51 via a cation-pi interaction (Fig. 34). The stable conformation of Arg54 of human NRS induces forced bending of the peptide backbone of Glu53-Arg54-Trp55 and the region forms a loop, while *Bm*NRS adopts an antiparallel β-sheet structure in the region. Together with the NMR titration results, the different conformation of the loop3 region may explain the target receptor specificity of UNE-Ns.

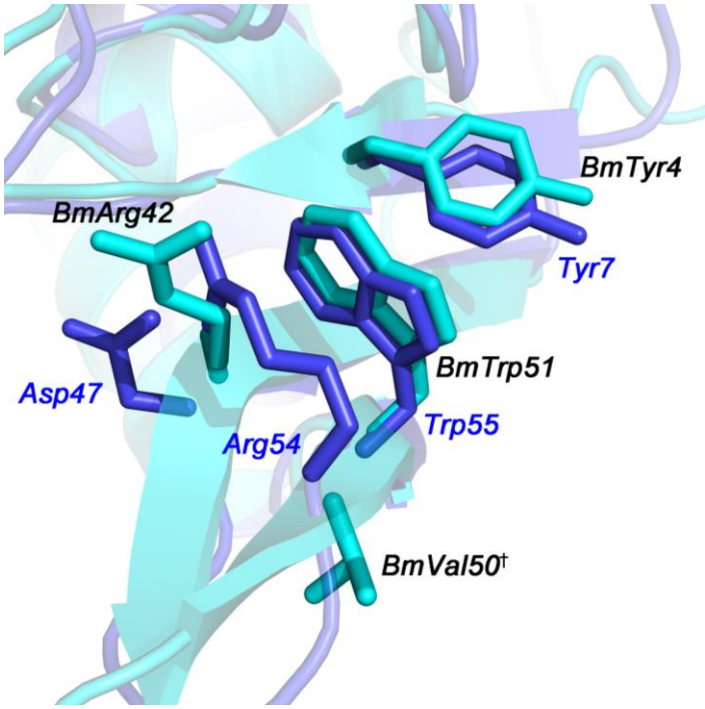

Figure 34. Residues on β2-loop3-β3 regions of UNE-Ns of human and *B. malayi*. Cα atoms of Trp55-Ser59 of human NRS and Trp51-Ser55 of *Bm*NRS are superposed. Human NRS and *Bm*NRS are colored in blue and cyan, respectively (*Bm*Val50†, Leu50 of *Bm*NRS was replaced with valine in NMR structure of *Bm*NRS).

4. Discussion

Evolutionary pressure to obtain novel functions in eukaryotic cell systems has resulted in the incorporation of non-translational additional domains into ARSs and has maintained ARS splicing variants with catalytic nulls[8,49]. In human NRS, domain addition at the N-terminus has been observed, but specific functional roles elicited by UNE-N remain unclear. Our crystal structure of UNE-N of NRS provides functional insight, as the overall structure was similar to the chemotactic UNE-N domain of *Bm*NRS which interacts with two chemokine receptors, CXCR1 and CXCR2.

The UNE-N domains of human NRS and *Bm*NRS are structurally similar and both exhibit non-translational chemokine activities that induce the migration of immune cells. Interestingly, structurally similar UNE-Ns from human NRS and *Bm*NRS target different chemokine receptors, CCR3 and CXCR1/2, respectively, and it is very important to elucidate how these structurally similar domains can recognize their matching receptors. To investigate how this novel domain fold interacts with chemokine receptors and why each UNE-N targets different receptors, I elucidated the interaction mode between UNE-N of NRS and CCR3 EDs by conducting pull-down assays and NMR perturbation experiments.

The results may not demonstrate a physical interaction between UNE-N and 'native' CCR3 but clearly show that UNE-N interacts with EDs derived from CCR3. If UNE-N did not interact with CCR3 at all, UNE-N would not be pulled down together with CCR3 EDs in the *in vitro* pull-down assay[50]. CCL5, a CCR3-targeting chemokine, was not pulled down together with MBP-fused CCR3 EDs. When chemokines binds to chemokine receptors, post-translational modifications such as tyrosine sulfation could be a key factor[51]. Thus, the interaction between CCL5 and MBP-fused CCR3 EDs in the pull-down assays might not be observed since MBP-fused CCR3 EDs were purified from *E. coli* and would not contain necessary post-translational modifications for the interaction.

In addition to the *in vitro* pull-down assays, NMR perturbation experiments were implemented with UNE-N and CCR3 EDs which further support the direct interaction between UNE-N and CCR3 EDs. NMR perturbation experiment was also used for the validation of interactions between CCR3 and CCL11 (eotaxin-1), a well-known CCR3 chemokine, in which a synthesized ED1 peptide derived from CCR3 was used[52]. Similarly, the interaction between CCL5 and CCR5 was investigated using peptides derived from CCR5 EDs[53]. Taken all together, the data from pull-down assays and NMR perturbation experiments would provide reliable evidences for the direct interaction between UNE-N and CCR3.

NMR perturbation experiment is a powerful tool as well for probing the interfaces of a protein with its binding partner[54-56]. According to the perturbation experiments for ^{15}N-labeled UNE-N with MBP-fused CCR3 EDs, peaks showing more sensitive broadening than other peaks were detected, which is often observed following titration with a protein ligand. However, the degree of chemical shift was not sufficient to assign specific residues affected by the titration experiments (Fig. 31 and Fig. 32). The degrees of peak broadening of UNE-N residues were affected by additions of CCR3 ED3, ED1, and ED2 in a descending order of reducing sensitivity while maintaining similar broadening patterns plotted by UNE-N residues. Residues in the loop3 region of UNE-N were mainly influenced by titrations with CCR3 EDs. For UNE-N of *Bm*NRS, the β2-loop3-β3-α2 motif has been suggested to interact with CXCR1/2 based on structural comparison with other chemokines[22]. The β2-loop3-β3 regions of UNE-N in NRS and *Bm*NRS are quite different in amino acid sequence and structure as described above. Thus, different conformations in the determinant β2-loop3-β3 region of UNE-Ns may mainly contribute to the selection of their target receptors.

Additionally, I found that Trp70 in human NRS, equivalent to Tyr66 in *Bm*NRS, is a highly conserved aromatic residue in helix α2 and forms a pi-pi interaction with Phe41 in the adjacent loop2, while Tyr66 in *Bm*NRS forms a pi-pi interaction with Trp63 in the same α2 helix (Fig. 35). This subtle structural difference may leave loop2 of *Bm*NRS more flexible[16] than that of human NRS, conferring an assistant role in recognizing target receptors (Fig. 36).

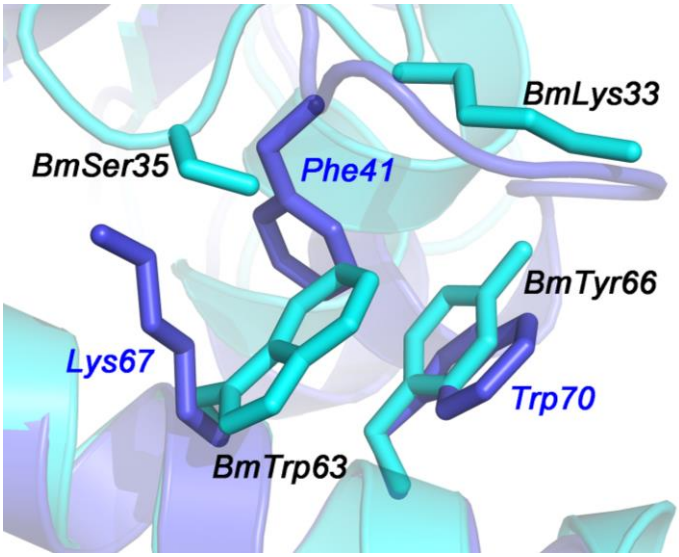

Figure 35. Residues on the loop2 and α2 regions of UNE-Ns of human and *B. malayi*. C_α atoms of Trp55-Ser59 of human NRS and Trp51-Ser55 of *Bm*NRS are superposed. Human NRS and *Bm*NRS are colored in blue and cyan, respectively.

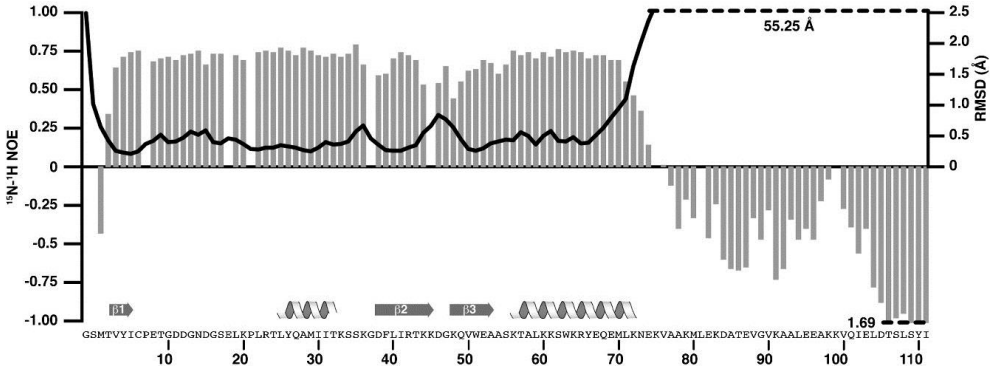

Figure 36. Backbone RMSD and ^{15}N–^{1}H hetero-nuclear NOE values of UNE-N of *Bm*NRS plotted against residue number. Loop2 and loop3 regions of UNE-N of *Bm*NRS show peaks in the backbone RMSD curve. (Reprinted from Crepin, T. et al. A hybrid structural model of the complete Brugia malayi cytoplasmic asparaginyl-tRNA synthetase. Journal of molecular biology 405, 1056-1069, doi:10.1016/j.jmb.2010.11.049 (2011), with permission from Elsevier)

The immunogenicity of antigenic materials interacting with receptors on antigen-presenting cells is highly augmented and the balance among immunomodulatory cytokines is a key factor in the life and death of cells [57,58]. As shown in the cell migration assays with UNE-N and other constructs of NRS, UNE-N exhibited chemokine activities in CCR3-expressing cells. Considering that autoantibodies against NRS have been detected in the sera of patients with autoimmune diseases such as ILD and myositis[46,59-62], the chemokine activity of NRS could be closely related to proinflammatory signaling. ILD is a well-known major clinical feature of patients with anti-KS and secreted NRS may elicit CCR3-mediated proinflammatory signaling in ILD development. And modulators of the NRS-CCR3 signaling axis may provide a niche for elucidating the mechanism of ILD and alleviating CCR3-mediated malignances.

Cytosolic NRS secretion from macrophages and specific targeting of CCR3 on immune cells may be explained as a "danger signal" from cells confronting stressful environments[18,63]. However, the exact roles of autoantibodies against secreted NRS and pathophysiological connections between NRS-CCR3 signaling and immune diseases require further investigations. Structural

information of UNE-N and CD of NRS at an atomic level and the interaction mode between UNE-N and CCR3 may provide a foundation for evaluating NRS-CCR3 signaling and its correlation with autoimmune diseases, in which development of anti-KS has been observed.

5. References

1. Eriani, G., Delarue, M., Poch, O., Gangloff, J. & Moras, D. Partition of tRNA synthetases into two classes based on mutually exclusive sets of sequence motifs. *Nature* **347**, 203-206, doi:10.1038/347203a0 (1990).

2. O'Donoghue, P. & Luthey-Schulten, Z. On the evolution of structure in aminoacyl-tRNA synthetases. *Microbiol Mol Biol Rev* **67**, 550-573 (2003).

3. Rajendran, V., Kalita, P., Shukla, H., Kumar, A. & Tripathi, T. Aminoacyl-tRNA synthetases: Structure, function, and drug discovery. *Int J Biol Macromol* **111**, 400-414, doi:10.1016/j.ijbiomac.2017.12.157 (2018).

4. Antonellis, A. & Green, E. D. The role of aminoacyl-tRNA synthetases in genetic diseases. *Annu Rev Genomics Hum Genet* **9**, 87-107, doi:10.1146/annurev.genom.9.081307.164204 (2008).

5. Lee, S. W., Cho, B. H., Park, S. G. & Kim, S. Aminoacyl-tRNA synthetase complexes: beyond translation. *J Cell Sci* **117**, 3725-3734, doi:10.1242/jcs.01342 (2004).

6. Guo, M., Schimmel, P. & Yang, X. L. Functional expansion of human tRNA synthetases achieved by structural inventions. *FEBS letters* **584**, 434-442, doi:10.1016/j.febslet.2009.11.064 (2010).

7. Kim, S., You, S. & Hwang, D. Aminoacyl-tRNA synthetases and tumorigenesis: more than housekeeping. *Nat Rev Cancer* **11**, 708-718, doi:10.1038/nrc3124 (2011).

8. Lo, W. S. *et al.* Human tRNA synthetase catalytic nulls with diverse functions. *Science* **345**, 328-332, doi:10.1126/science.1252943 (2014).

9. Kyriacou, S. V. & Deutscher, M. P. An important role for the multienzyme aminoacyl-tRNA synthetase complex in mammalian translation and cell growth. *Mol Cell* **29**, 419-427, doi:10.1016/j.molcel.2007.11.038 (2008).

10. Ray, P. S., Arif, A. & Fox, P. L. Macromolecular complexes as depots for releasable regulatory proteins. *Trends Biochem Sci* **32**, 158-164, doi:10.1016/j.tibs.2007.02.003 (2007).

11. Cusack, S., Hartlein, M. & Leberman, R. Sequence, structural and evolutionary relationships between class 2 aminoacyl-tRNA synthetases. *Nucleic acids research* **19**, 3489-3498 (1991).

12. Reed, V. S. & Yang, D. C. Characterization of a novel N-terminal peptide in human aspartyl-tRNA synthetase. Roles in the transfer of aminoacyl-tRNA from aminoacyl-tRNA synthetase to the elongation factor 1 alpha. *The Journal of biological chemistry* **269**, 32937-32941 (1994).

13. Rees, B., Cavarelli, J. & Moras, D. Conformational flexibility of tRNA: structural changes in yeast tRNA(Asp) upon binding to aspartyl-tRNA synthetase. *Biochimie* **78**, 624-631 (1996).

14. Francin, M., Kaminska, M., Kerjan, P. & Mirande, M. The N-terminal domain of mammalian Lysyl-tRNA synthetase is a functional tRNA-binding domain. *The Journal of biological chemistry* **277**, 1762-1769, doi:10.1074/jbc.M109759200 (2002).

15. Cheong, H. K. *et al.* Structure of the N-terminal extension of human aspartyl-tRNA synthetase: implications for its biological function. *Int J Biochem Cell Biol* **35**, 1548-1557 (2003).

16. Crepin, T. *et al.* A hybrid structural model of the complete Brugia malayi cytoplasmic asparaginyl-tRNA synthetase. *Journal of molecular biology* **405**, 1056-1069, doi:10.1016/j.jmb.2010.11.049 (2011).

17. Kim, K. R. *et al.* Crystal structure of human cytosolic aspartyl-tRNA synthetase, a component of multi-tRNA synthetase complex. *Proteins* **81**, 1840-1846, doi:10.1002/prot.24306 (2013).

18. Howard, O. M. Z. *et al.* Histidyl-tRNA Synthetase and Asparaginyl-tRNA Synthetase, Autoantigens in Myositis, Activate Chemokine Receptors on T Lymphocytes and Immature Dendritic Cells. *Journal of Experimental Medicine* **196**, 781-791, doi:10.1084/jem.20020186 (2002).

19. Ramirez, B. L. *et al.* Brugia malayi asparaginyl-transfer RNA synthetase induces chemotaxis of human leukocytes and activates G-protein-coupled receptors CXCR1 and CXCR2. *J Infect Dis* **193**, 1164-1171, doi:10.1086/501369 (2006).

20. Kron, M., Marquard, K., Hartlein, M., Price, S. & Leberman, R. An immunodominant antigen of Brugia malayi is an asparaginyl-tRNA synthetase. *FEBS letters* **374**, 122-124 (1995).

21. Kron, M., Petridis, M., Milev, Y., Leykam, J. & Hartlein, M. Expression, localization and alternative function of cytoplasmic asparaginyl-tRNA synthetase in Brugia malayi. *Molecular and biochemical parasitology* **129**, 33-39 (2003).

22. Kron, M. A., Wang, C., Vodanovic-Jankovic, S., Howard, O. M. & Kuhn, L. A. Interleukin-8-like activity in a filarial asparaginyl-tRNA synthetase. *Molecular and biochemical parasitology* **185**, 66-69, doi:10.1016/j.molbiopara.2012.06.003 (2012).

23. D, J. J. *et al.* Brugia malayi Asparaginyl-tRNA Synthetase Stimulates Endothelial Cell Proliferation, Vasodilation and Angiogenesis. *PLoS One* **11**, e0146132, doi:10.1371/journal.pone.0146132 (2016).

24. Manole, C., Inimioara Mihaela, C. & Bogdan, C. New Insights into Antisynthetase Syndrome. *Maedica (Buchar)* **11**, 130-135 (2016).

25. Mahler, M., Miller, F. W. & Fritzler, M. J. Idiopathic inflammatory myopathies and the anti-synthetase syndrome: a comprehensive review. *Autoimmun Rev* **13**, 367-371, doi:10.1016/j.autrev.2014.01.022 (2014).

26. Hamaguchi, Y. *et al.* Common and distinct clinical features in adult patients with anti-aminoacyl-tRNA synthetase antibodies: heterogeneity within the syndrome. *PLoS One* **8**, e60442, doi:10.1371/journal.pone.0060442 (2013).

27. Plotz, P. H. The autoantibody repertoire: searching for order. *Nat Rev Immunol* **3**, 73-78, doi:10.1038/nri976 (2003).

28. Park, M. C. *et al.* Secreted human glycyl-tRNA synthetase implicated in defense against ERK-activated tumorigenesis. *Proceedings of the National Academy of Sciences of the United States of America* **109**, E640-647, doi:10.1073/pnas.1200194109 (2012).

29. Fernandez, E. J. & Lolis, E. Structure, function, and inhibition of chemokines. *Annu Rev Pharmacol Toxicol* **42**, 469-499, doi:10.1146/annurev.pharmtox.42.091901.115838 (2002).

30. Daugherty, B. L. *et al.* Cloning, expression, and characterization of the human eosinophil eotaxin receptor. *J Exp Med* **183**, 2349-2354 (1996).

31. Slabinski, L. *et al.* XtalPred: a web server for prediction of protein crystallizability. *Bioinformatics* **23**, 3403-3405, doi:10.1093/bioinformatics/btm477 (2007).

32. Otwinowski, Z. & Minor, W. [20] Processing of X-ray diffraction data collected in oscillation mode. *Methods in enzymology* **276**, 307-326, doi:10.1016/S0076-6879(97)76066-X (1997).

33. Adams, P. D. *et al.* PHENIX: a comprehensive Python-based system for macromolecular structure solution. *Acta Crystallogr D Biol Crystallogr* **66**, 213-221, doi:10.1107/S0907444909052925 (2010).

34. Terwilliger, T. C. SOLVE and RESOLVE: automated structure solution and density modification. *Methods Enzymol* **374**, 22-37, doi:10.1016/S0076-6879(03)74002-6 (2003).

35. McCoy, A. J. *et al.* Phaser crystallographic software. *J Appl Crystallogr* **40**, 658-674, doi:10.1107/S0021889807021206 (2007).

36. Vagin, A. & Teplyakov, A. Molecular replacement with MOLREP. *Acta crystallographica. Section D, Biological crystallography* **66**, 22-25, doi:10.1107/S0907444909042589 (2010).

37. Emsley, P., Lohkamp, B., Scott, W. G. & Cowtan, K. Features and development of Coot. *Acta Crystallogr D Biol Crystallogr* **66**, 486-501, doi:10.1107/S0907444910007493 (2010).

38. Afonine, P. V. *et al.* Towards automated crystallographic structure refinement with phenix.refine. *Acta Crystallogr D Biol Crystallogr* **68**, 352-367, doi:10.1107/S0907444912001308 (2012).

39. Chen, V. B. *et al.* MolProbity: all-atom structure validation for macromolecular crystallography. *Acta Crystallogr D Biol Crystallogr* **66**, 12-21, doi:10.1107/S0907444909042073 (2010).

40. Kabsch, W. & Sander, C. Dictionary of protein secondary structure: pattern recognition of hydrogen-bonded and geometrical features. *Biopolymers* **22**, 2577-2637, doi:10.1002/bip.360221211 (1983).

41. Touw, W. G. *et al.* A series of PDB-related databanks for everyday needs. *Nucleic acids research* **43**, D364-368, doi:10.1093/nar/gku1028 (2015).

42. Delaglio, F. *et al.* NMRPipe: a multidimensional spectral processing system based on UNIX pipes. *J Biomol NMR* **6**, 277-293 (1995).

43. Shen, Y., Delaglio, F., Cornilescu, G. & Bax, A. TALOS+: a hybrid method for predicting protein backbone torsion angles from NMR chemical shifts. *J Biomol NMR* **44**, 213-223, doi:10.1007/s10858-009-9333-z (2009).

44. Holm, L. & Rosenstrom, P. Dali server: conservation mapping in 3D. *Nucleic acids research* **38**, W545-549, doi:10.1093/nar/gkq366 (2010).

45. Krissinel, E. & Henrick, K. Inference of macromolecular assemblies from crystalline state. *Journal of molecular biology* **372**, 774-797, doi:10.1016/j.jmb.2007.05.022 (2007).

46. Hirakata, M. *et al.* Anti-KS: identification of autoantibodies to asparaginyl-transfer RNA synthetase associated with interstitial lung disease. *J Immunol* **162**, 2315-2320 (1999).

47. Son, S. H., Park, M. C. & Kim, S. Extracellular activities of aminoacyl-tRNA synthetases: new mediators for cell-cell communication. *Top Curr Chem* **344**, 145-166, doi:10.1007/128_2013_476 (2014).

48. Gallivan, J. P. & Dougherty, D. A. Cation-pi interactions in structural biology. *Proceedings of the National Academy of Sciences of the United States of America* **96**, 9459-9464 (1999).

49. Guo, M., Yang, X. L. & Schimmel, P. New functions of aminoacyl-tRNA synthetases beyond translation. *Nat Rev Mol Cell Biol* **11**, 668-674, doi:10.1038/nrm2956 (2010).

50. Louche, A., Salcedo, S. P. & Bigot, S. Protein-Protein Interactions: Pull-Down Assays. *Methods Mol Biol* **1615**, 247-255, doi:10.1007/978-1-4939-7033-9_20 (2017).

51. Ludeman, J. P. & Stone, M. J. The structural role of receptor tyrosine sulfation in chemokine recognition. *Br J Pharmacol* **171**, 1167-1179, doi:10.1111/bph.12455 (2014).

52. Millard, C. J. *et al.* Structural basis of receptor sulfotyrosine recognition by a CC chemokine: the N-terminal region of CCR3 bound to CCL11/eotaxin-1. *Structure* **22**, 1571-1581, doi:10.1016/j.str.2014.08.023 (2014).

53. Duma, L., Haussinger, D., Rogowski, M., Lusso, P. & Grzesiek, S. Recognition of RANTES by extracellular parts of the CCR5 receptor. *Journal of molecular biology* **365**, 1063-1075, doi:10.1016/j.jmb.2006.10.040 (2007).

54. McAlister, M. S. *et al.* NMR analysis of interacting soluble forms of the cell-cell recognition molecules CD2 and CD48. *Biochemistry* **35**, 5982-5991, doi:10.1021/bi952756u (1996).

55. Zuiderweg, E. R. Mapping protein-protein interactions in solution by NMR spectroscopy. *Biochemistry* **41**, 1-7 (2002).

56. Davis, S. J., Davies, E. A., Tucknott, M. G., Jones, E. Y. & van der Merwe, P. A. The role of charged residues mediating low affinity protein-protein recognition at the cell surface by CD2. *Proceedings of the National*

Academy of Sciences of the United States of America **95**, 5490-5494 (1998).

57. Henry, F. *et al.* Antigen-presenting cells that phagocytose apoptotic tumor-derived cells are potent tumor vaccines. *Cancer Res* **59**, 3329-3332 (1999).

58. Ronchetti, A. *et al.* Immunogenicity of apoptotic cells in vivo: role of antigen load, antigen-presenting cells, and cytokines. *J Immunol* **163**, 130-136 (1999).

59. Targoff, I. N. Update on myositis-specific and myositis-associated autoantibodies. *Curr Opin Rheumatol* **12**, 475-481 (2000).

60. Hengstman, G. J., van Engelen, B. G., Vree Egberts, W. T. & van Venrooij, W. J. Myositis-specific autoantibodies: overview and recent developments. *Curr Opin Rheumatol* **13**, 476-482 (2001).

61. Schneider, F. *et al.* The pulmonary histopathology of anti-KS transfer RNA synthetase syndrome. *Arch Pathol Lab Med* **139**, 122-125, doi:10.5858/arpa.2013-0667-OA (2015).

62. Hirakata, M. *et al.* Clinical and immunogenetic features of patients with autoantibodies to asparaginyl-transfer RNA synthetase. *Arthritis Rheum* **56**, 1295-1303, doi:10.1002/art.22506 (2007).

63. Gallucci, S. & Matzinger, P. Danger signals: SOS to the immune system. *Curr Opin Immunol* **13**, 114-119 (2001).

6. 국문 초록

Antisynthetase syndrome 은 autoimmune disease 의 하나로, aminoacyl-tRNA synthetase 에 대한 antibody 가 만들어진다. 그 중에서 asparaginyl-tRNA synthetase 에 대한 autoantibody 인 anti-KS 의 발생은 interstitial lung disease 와 밀접한 관련이 있는 것으로 보이는데 아직 생성 기전이 명확하게 밝혀지지 않았다.

본 연구에서는 human asparaginyl-tRNA synthetase 의 N 말단 부위의 결정구조를 규명하였고 그 구조가 *Brugia malayi* asparaginyl-tRNA synthetase 의 N 말단 부위와 유사하다는 것을 밝혔다. 또한 human asparaginyl-tRNA synthetase 의 N 말단 부위가 CC chemokine receptor 3 와 직접 결합하여 독립적으로 chemokine 활성을 가진다는 것을 보였고, 그 결합 방식을 NMR spectroscopy 기법을 이용하여 설명하였다.

나아가, interstitial lung disease 의 발달과 autoantibody 의 생성에 있어 human asparaginyl-tRNA synthetase 의 증가된 분비에 따른 비정상적인 N 말단 부위의 chemokine 활성이 잠재적 역할을 할 것이라 제시하였다.

주요 단어: Human asparaginyl-tRNA synthetase (NRS), chemokine, CC chemokine receptor 3 (CCR3), X-ray crystallography, antisynthetase syndrome

학번: 2012-21588

Acknowledgements

I first thank my supervisor, Prof. Byung Woo Han, for his teaching and support during my Ph.D. course. And I thank my thesis committee, Prof. Jung Weon Lee, Prof. Sunghoon Kim, Prof. Bong-Jin Lee, and Prof. Jin Kuk Yang for their comments and support to my dissertation. I also thank Prof. Hyun-Jung Kim for review of my study, Dr. Min Chul Park, Dr. Peter C. Goughnour, and Dr. Seung Jae Jeong for cell-based assay and pull-down assay, Dr. Ki-Young Lee for NMR study, Dr. Hyoun Sook Kim for x-ray crystallography, and Prof. Jae-Young Lee for statistical analysis. Lastly, I thank the staff of the beamlines, PLS-5C of Pohang Accelerator Laboratory (Pohang, Republic of Korea) and AR-NW12A of Photon Factory (Tsukuba, Japan), for x-ray diffraction experiments.